Supporting Information

Synergistic Coupling of Anionic Ligands to Optimize the Electronic and Catalytic Properties of Metal-Organic Framework-Converted Oxygen-Evolving Catalysts

Wenhui He,[a] Hui-Min Gao,[b] Ran Shimoni,[a] Zhong-Yuan Lu,[b] and Idan Hod [a]*

[a] Department of Chemistry and Ilse Katz Institute for Nanoscale Science and Technology, Ben-Gurion University of Negev, Beer-Sheva, 8410501, Israel

[b] State Key Laboratory of Supramolecular Structure and Materials, Institute of Theoretical Chemistry, Jilin University, Changchun, 130021, China

***Corresponding Author** Idan Hod, E-mail: hodi@bgu.ac.il

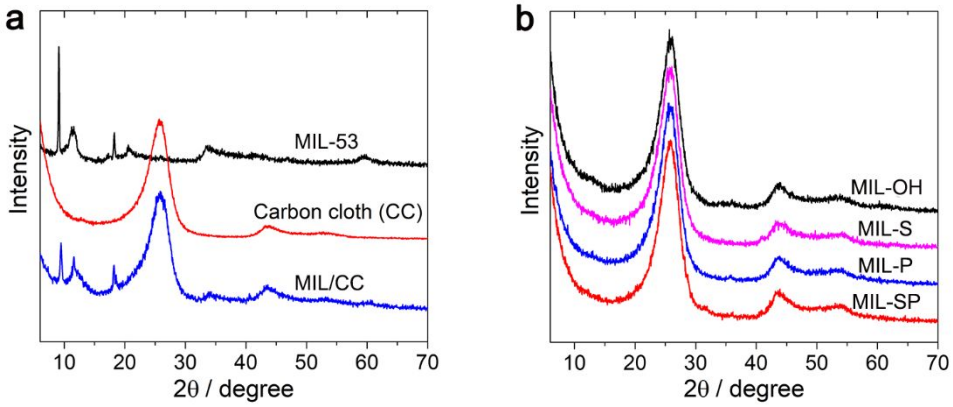

Figure S1. XRD patterns: (a) MIL-53 powder, carbon cloth (CC), and MIL-53 loaded on CC (MIL/CC); (b) the as-prepared MOFs (MIL-53)-derived materials.

In **Figure S1b**, the MIL-53 derived materials only show the XRD patterns of the carbon cloth supports, indicating that the crystalline MIL-53 has been electrochemically converted into amorphous metal oxides/hydroxides (MIL-OH) and sulfides (MIL-S). After low-temperature phosphorization, the MIL-P and MIL-SP also show featureless XRD patterns, which should be due to their structure assembled by ultra-small nanoparticles, as evidenced by the TEM images of MIL-SP (**Figure S12 and Figure S13**).

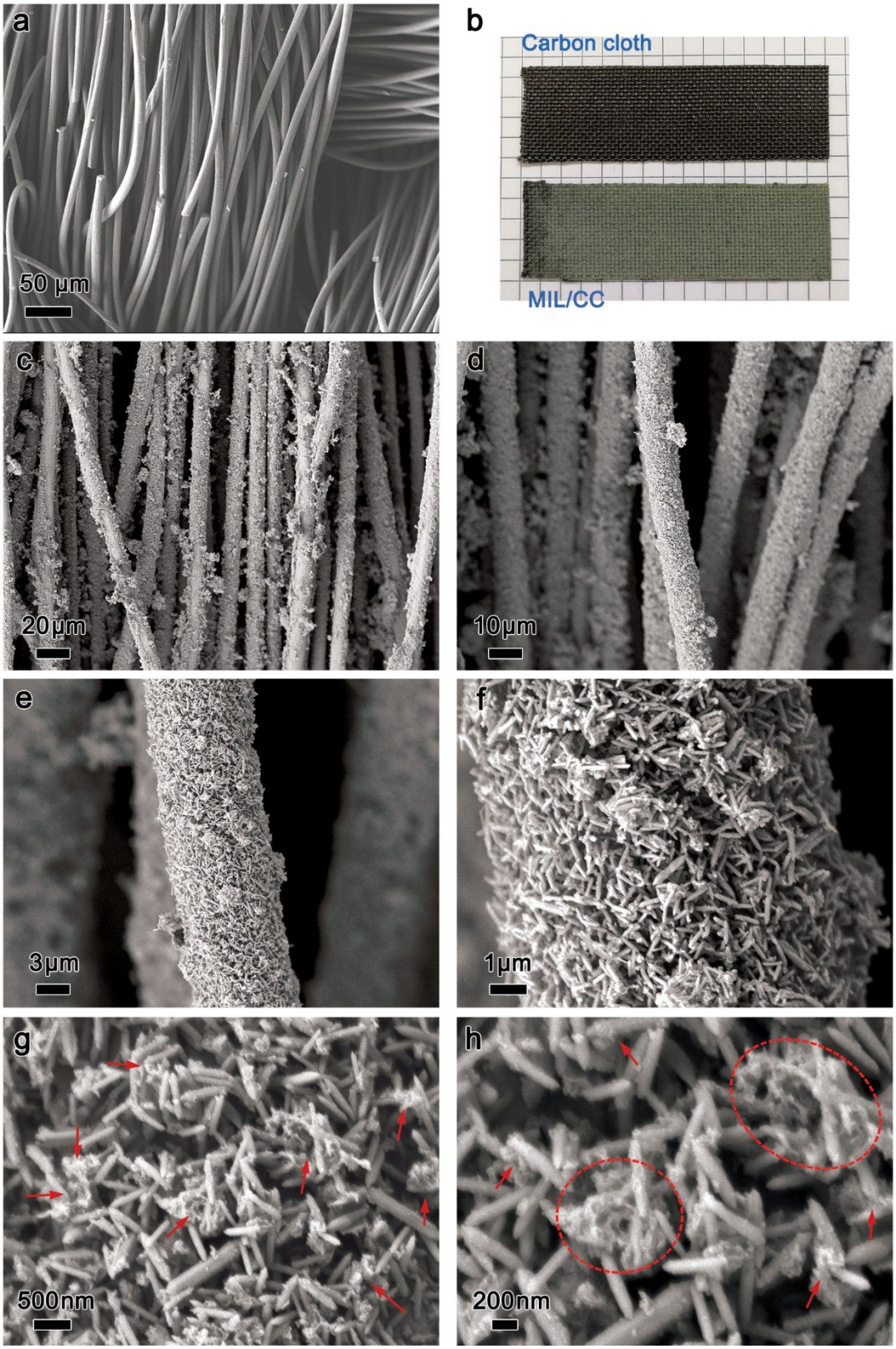

Figure S2. (a) SEM images of carbon cloth substrate, (b) Photographs of carbon cloth (up) and MIL/CC (bottom) prepared by electrophoretic deposition (EPD) of MIL-53 onto carbon cloth (CC). (c-h) SEM images of MIL/CC in different magnification.

As shown in **Figure S2c** and **Figure S2d**, the carbon cloth fiber is uniformly covered by MIL-53 particles (an average length of *ca.* 1μm and diameter of 150 nm), which are jointed by porous granular binders derived from Ni^{2+} hydrolysis upon EPD (red arrows and cycles in **Figure S2g** and **Figure S2h**). Remarkably, these Ni^{2+}-derived granular binders will disappear

in the MOF-derived products after electrochemical conversion (MIL-OH in **Figure S6** and MIL-S in **Figure S7**). This result indicates that these binders actually worked as electrochemically-active joints and were built into MOF-derived networks during the electrochemical conversion processes. This morphology evolvement provides a view for understanding the forming mechanism of the unique 3D-interconnected networks of the MOF-derived products (MIL-OH and MIL-S).

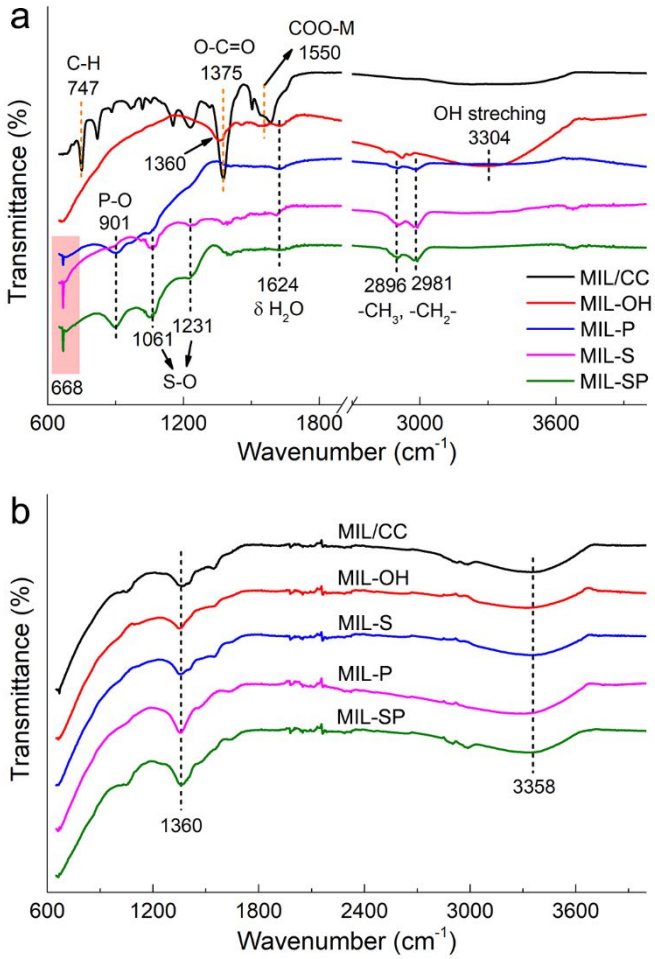

Figure S3. FT-IR absorbance spectra: (a) the as-prepared samples before OER tests; (b) the samples after OER tests. The OER tests here contain the initial Linear sweep voltammetry (LSV) tests (from 0.9 V_{RHE} to 2.1 V_{RHE}), and CV tests (from 0.9 V_{RHE} to1.6 V_{RHE}), which were conducted at a scan rate of 2 mV/s and 10 mV/s, respectively. Both the LSV and CV tests were continuously performed until the LSV and CV curves had no observable change.

As shown in **Figure S3a**, the MIL/CC has the characteristic FT-IR signals of the organic ligands (benzene dicarboxylic acid, BDC) and the bonding metal-carboxyl group of MIL-53.[1] After EC-MOF processes (MIL-OH and MIL-S), the above-mentioned signals basically disappeared, accompanying with the emerging of new signals related to metal sulfide (668 cm^{-1}) and S-O bond (1061 and 1231 cm^{-1}).[2,3] The FT-IR absorbance peak at 1360 cm^{-1} (MIL-OH) is from the absorbed CO_3^{2-} on the surface metal sites of Fe/Ni(OOH)x.[4] These results suggest that the BDC ligands in MIL/CC were basically replaced by O^{2-}/OH^- and S^{2-} ligands, and were then released into the electrolyte. After phosphorization, a new peak at ~901 cm^{-2} appeared in the FT-IR of MIL-P and MIL-SP, which might be related to the PO_x and/or metal phosphides.

After OER tests (**Figure S3b**), the FT-IR spectra of all the samples tended to be similar. Their same peaks at 1360 cm^{-1} and 3358 cm^{-1} correspond to the absorbed CO_3^{2-} and H_2O, respectively.[4] This result indicates that the surface of the samples after OER tests was oxidized and/or reconstructed to expose Fe/Ni oxyhydroxide.

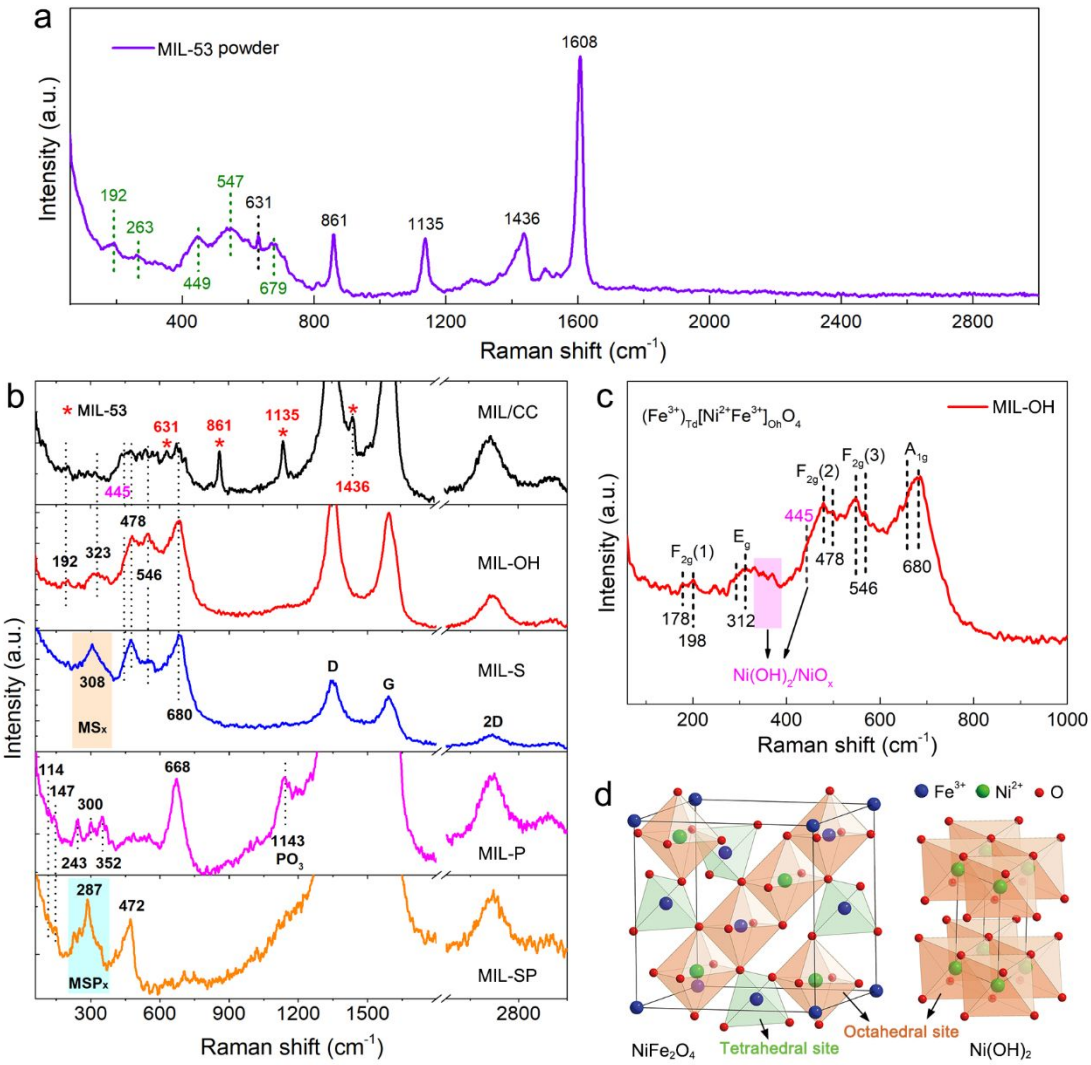

Figure S4. Raman spectra: (a) (Ni, Fe)-MIL-53 powders, (b) the (Ni, Fe)-MIL-53 derived products, (c) a magnified Raman spectra of MIL-OH in (b). (d) Schematic of a representative inverse spinel structure of $NiFe_2O_4$ and a layer-like structure of $Ni(OH)_2$, showing oxygen atoms (red), tetrahedral (orange), octahedral (light green) units. The structure was drawn using the DIAMOND software.

In **Figure S4a**, MIL-53 powders show two sets of Raman peaks: the green numbers should be from the metal nodes of MIL-53, which is very similar to the Raman signals of $Ni(OH)_2$ (449 cm^{-1})/$FeNiOH_x$ (547 and 679 cm^{-2});[5-7] the black numbers should be from the organic ligands and/or the bonds of metal-ligands. In **Figure S4b**, MIL/CC also show a set of peaks (red stars) related to the organic ligands. Meanwhile, the Raman signals related to the metal nodes tend to be a broad peak, which may be due to the deposition of some $Ni(OH)_x$ (445 cm^{-1})/NiO_x (500 cm^{-1}) binders upon EPD.[6] The Raman peaks at 1348 cm^{-1}, 1592 cm^{-1} and 2693 cm^{-1} is from the D, G, and 2D modes of graphitic carbon cloths.[8] After electrochemical conversion, the set of red star-marked peaks in MIL/CC disappeared in the Raman spectra of MIL-OH and MIL-S, suggesting the BDC organic ligands is replaced by OH^-/O^{2-} or S^{2-} ligands.

In **Figure S4c**, a close look at the Raman modes of MIL-OH, together with its composition, reveal the presence of $NiFe_2O_4$ phase with inverse spinel structure (O_7^h (Fd3m) space group with 5 theoretically-predicted Raman active modes: A_{1g}+E_g+3F_{2g}) and $Ni(OH)_2$/NiO_x phase.[9-11] This result implies that Ni^{2+} in MIL-OH actually exist in two different coordination environments,

well in consistent with the CV tests (**Figure S17 and Figure S18**). In **Figure S4b**, similar Raman signals of spinel phase in MIL-S should be derived from the surface oxidation of corresponding metal sulfides (MS_x, 308 cm^{-1}).[3] In contrast, the Raman modes of original MIL-P and MIL-SP can't be indexed to the spinel structure, but the Raman peaks of MIL-P after OER clearly prove the reorganization of spinel phase on their surface (**Figure S5**). The same situation occurs on the MIL/CC. In **Figure S5**, the MIL-SP after OER doesn't show the complete Raman modes of spinel phase, which may be due to its higher stability against oxidation, as supported by the following XPS measurements (**Figure S28** and **Figure 29**).

This preferential formation spinel phase ($NiFe_2O_4$, Ni : Fe = 1:2) in MOF-derived catalysts can be partially attributed to the unevenly-distributed Ni^{2+} and Fe^{3+} ions in the MIL-53 precursors, as evidenced by the different Ni/Fe atomic ratio between ICP and EDX data (**Table S1**), while the coexistence of two Ni^{2+} coordination environments should be due to the atomic ratio of Ni/Fe (~2:1) on the surface layer of catalysts, as determined by the EDX spectra (**Figure S8** and **Figure S11**).

As shown in **Figure S4d**, based on the inverse spinel structure of $NiFe_2O_4$ phase, the tetrahedral (T_e) sites are occupied by one and half of the Fe^{3+} ions, while the other half of the Fe^{3+} and Ni^{2+} ions are distributed over the octahedral (O_c) sites (Figure 3a).[9,10] In contrast, the Ni^{2+} ions in the $Ni(OH)_2$ exclusively occupies the O_c sites. Importantly, it is suggested that the O_c sites are catalytic active, whereas the T_e sites are almost inert.[12] Hence, both the Fe^{3+} and Ni^{2+} ions occupying O_c sites might account for the apparent OER activities of the MOF-derived catalysts.

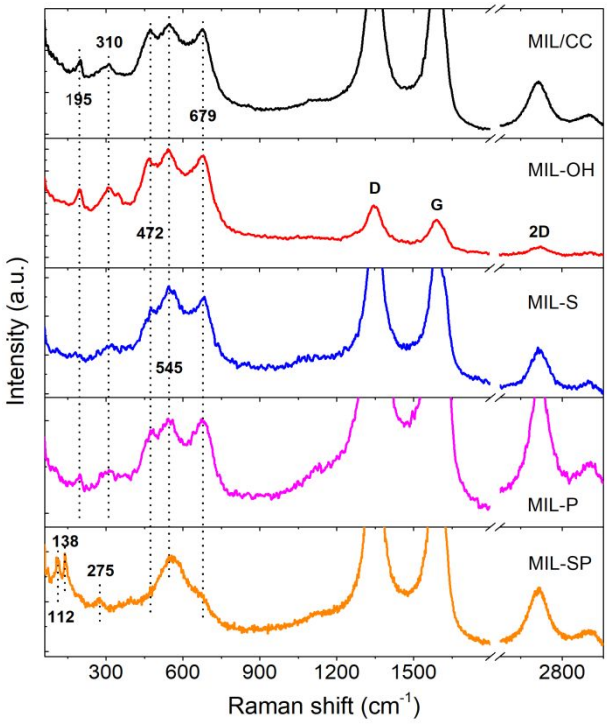

Figure S5. Raman spectra of the samples after OER tests. The OER tests taken here is similar to that before the FT-IR measurements (Fig. S3b).

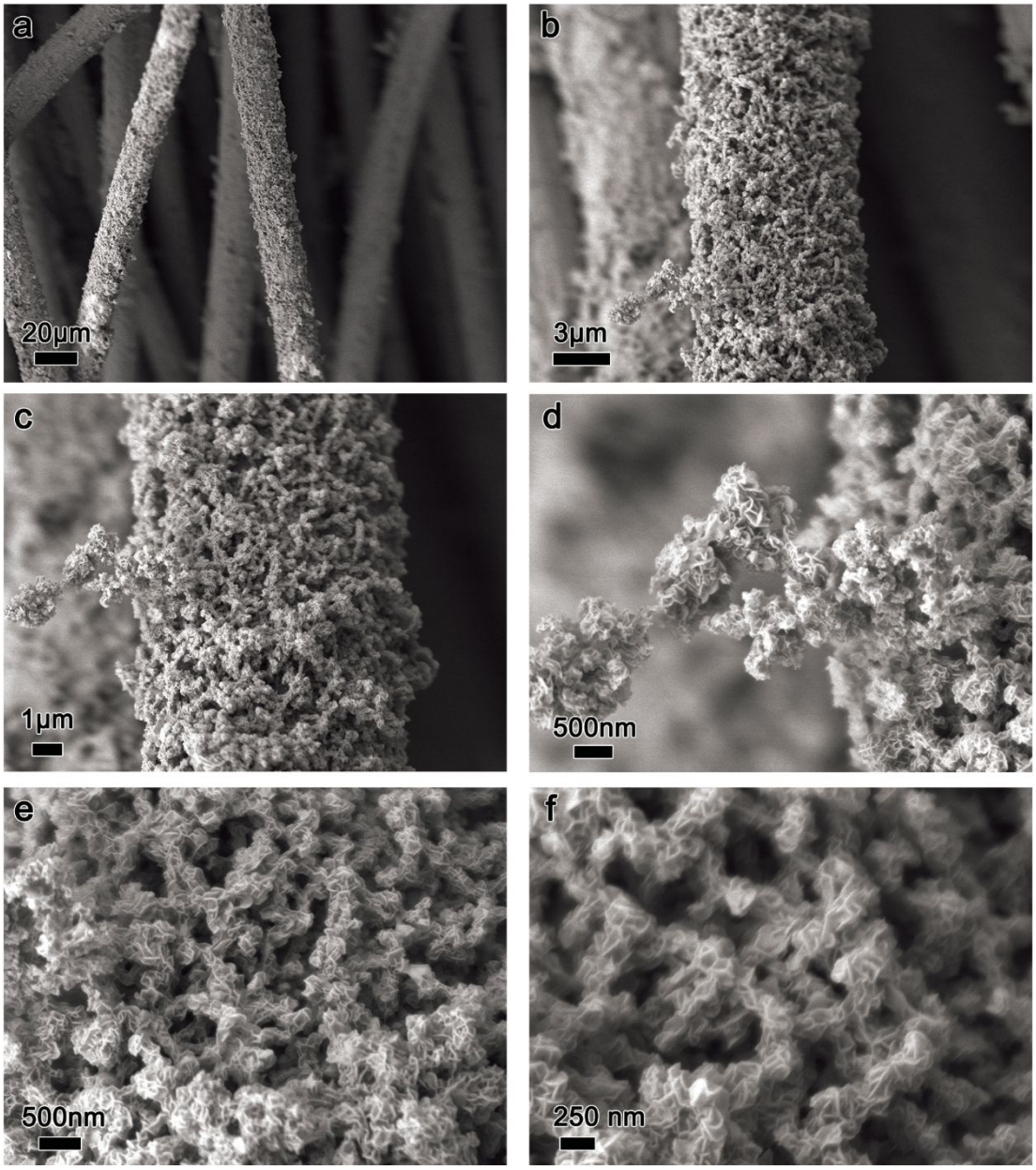

Figure S6. (a-f) SEM images of the **MIL-OH** with different levels of magnification.

The SEM images, especially the **Fig. S6d**, suggest that the MIL-53 precursors themselves are well electrochemically interconnected and also have good electron contact with carbon cloth support, leading to the even formation and distribution of the nanosheet products. This result firmly demonstrates the remarkable advantages of our elaborately-designed electrophoretic deposition (EPD) and electrochemical conversion of MOFs (EC-MOF) methods.

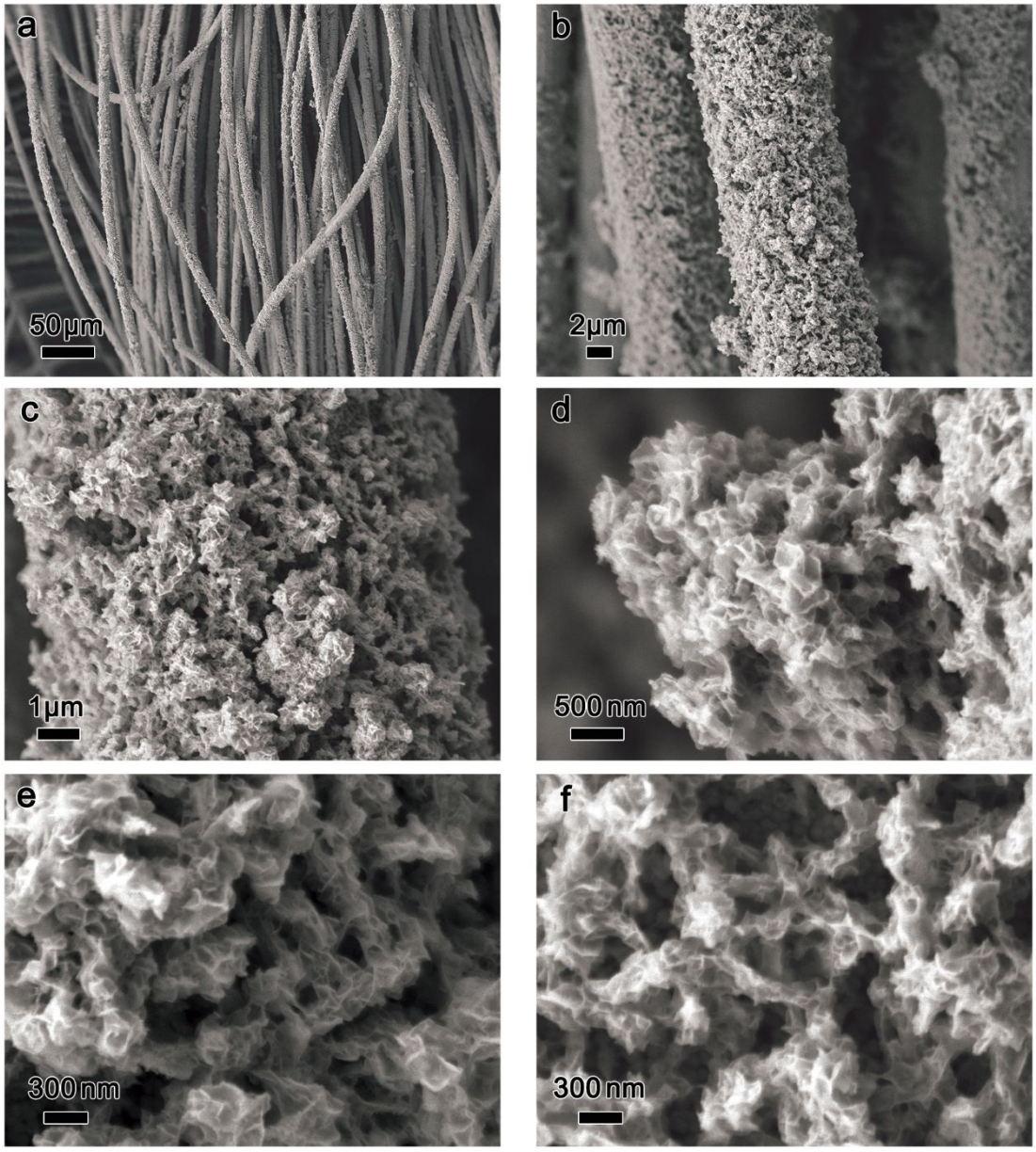

Figure S7. (a-f) SEM images of the **MIL-S** with different levels of magnification.

Similar to MIL-OH, the MIL-S also exhibits a 3D-hierarchical network structure, but the assembled nanosheets on MIL-S is a litter larger than that of MIL-OH, which might be due to a better electron conductivity of the formed metal sulfides in MIL-S during the EC-MOF processes.

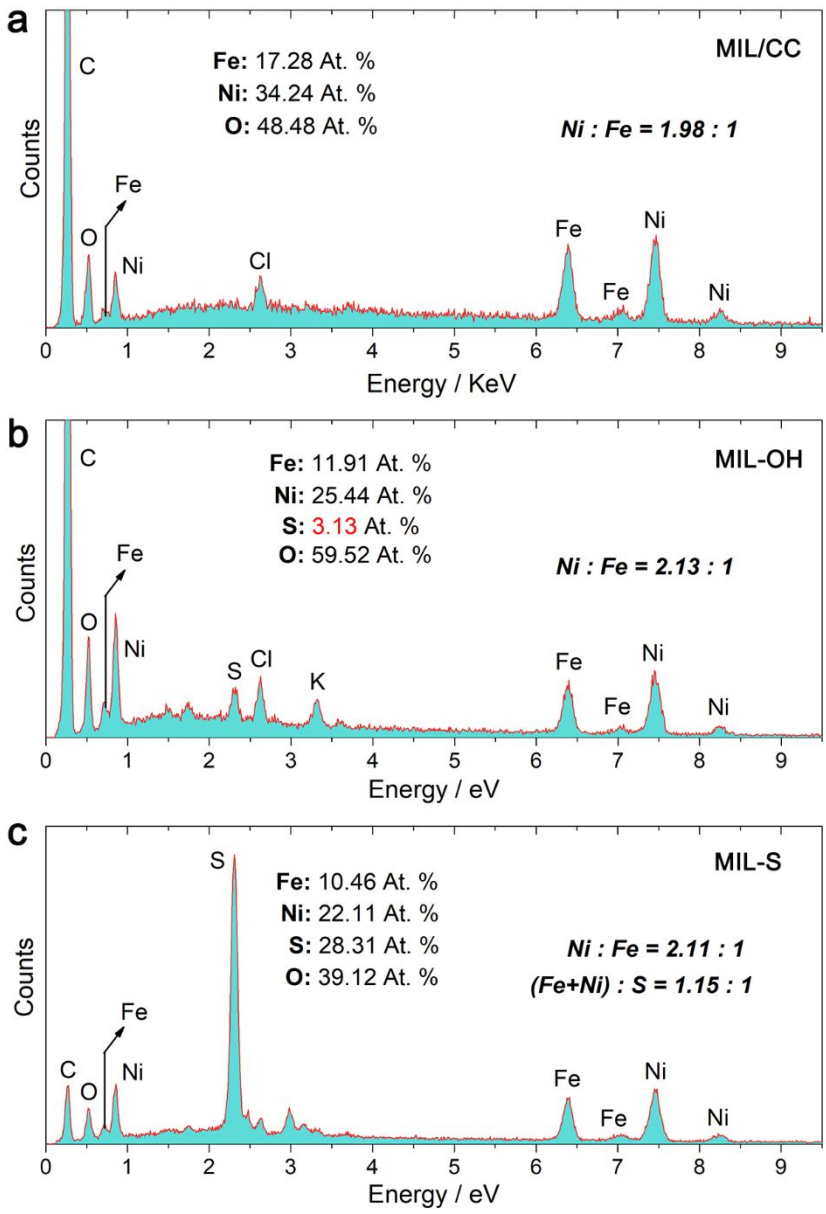

Figure S8. Energy dispersive X-ray (EDX) spectrum of (a) MIL/CC, (b) MIL-OH, and (c) MIL-S.

EDX spectrum reveals the close Ni/Fe atomic ratios (~2:1) in the MIL/CC and its electrochemically converted products (MIL-OH and MIL-S). This result suggests that the Ni^{2+} and Fe^{3+} ions in the MIL/CC precursors could be basically retained during the EC-MOF processes. Remarkably, the slightly larger Ni/Fe atomic ratio on the MIL-OH (2.13:1) and MIL-S (2.23:1) than that on the MIL/CC (1.98:1) might be due to the redistribution of Ni^{2+}-derived granular binders (formed upon the EPD, **Figure S2**) during the EC-MOF processes. This deduction can be supported by the disappearance of these Ni^{2+}-derived granular binders in the SEM images of MIL-OH (**Figure S6**) and MIL-S (**Figure S7**). Thus, these binders could work as electrochemically-active joints and were built onto MOF-derived networks during the EC-MOF processes. In MIL-S, the ratio of metal and S ligands is close to 1:1, indicating the formation of metal sulfides. Remarkably, there is still a certain amount of O species in MIL-S (**Fig. S8c**), which may be from the surface oxidized S (SO_x) and certain residual oxide species. Note that O doping in amorphous metal sulfides have been verified to optimize the electronic structure of metal center and improve the anti-oxidation ability of M-S bonds in metal sulfides during OER.[13,14] Few S species detected in MIL-OH might be from the left S contaminants in the electrochemical cells.

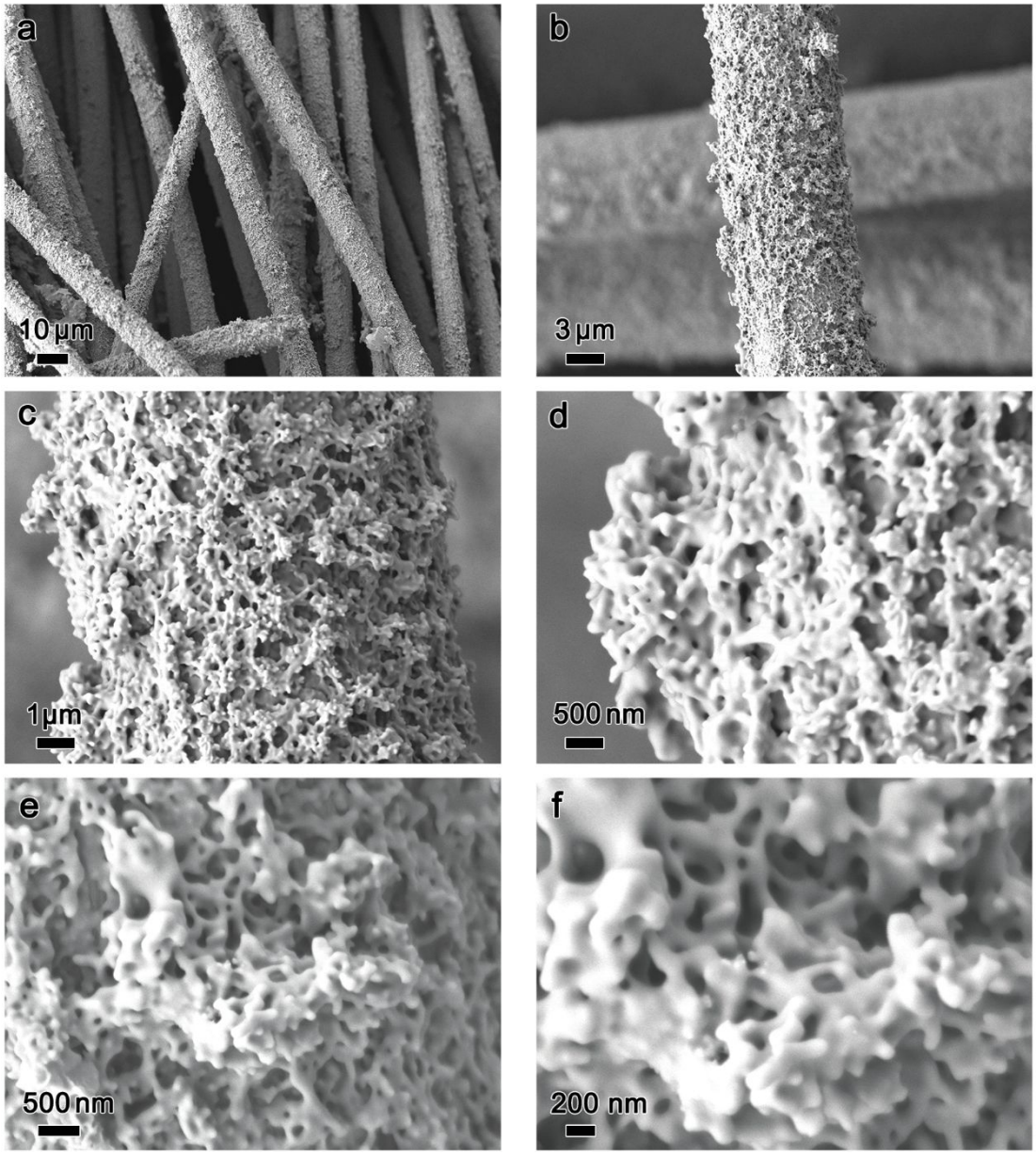

Figure S9. SEM images of the **MIL-P** (a-f) with different levels of magnification.

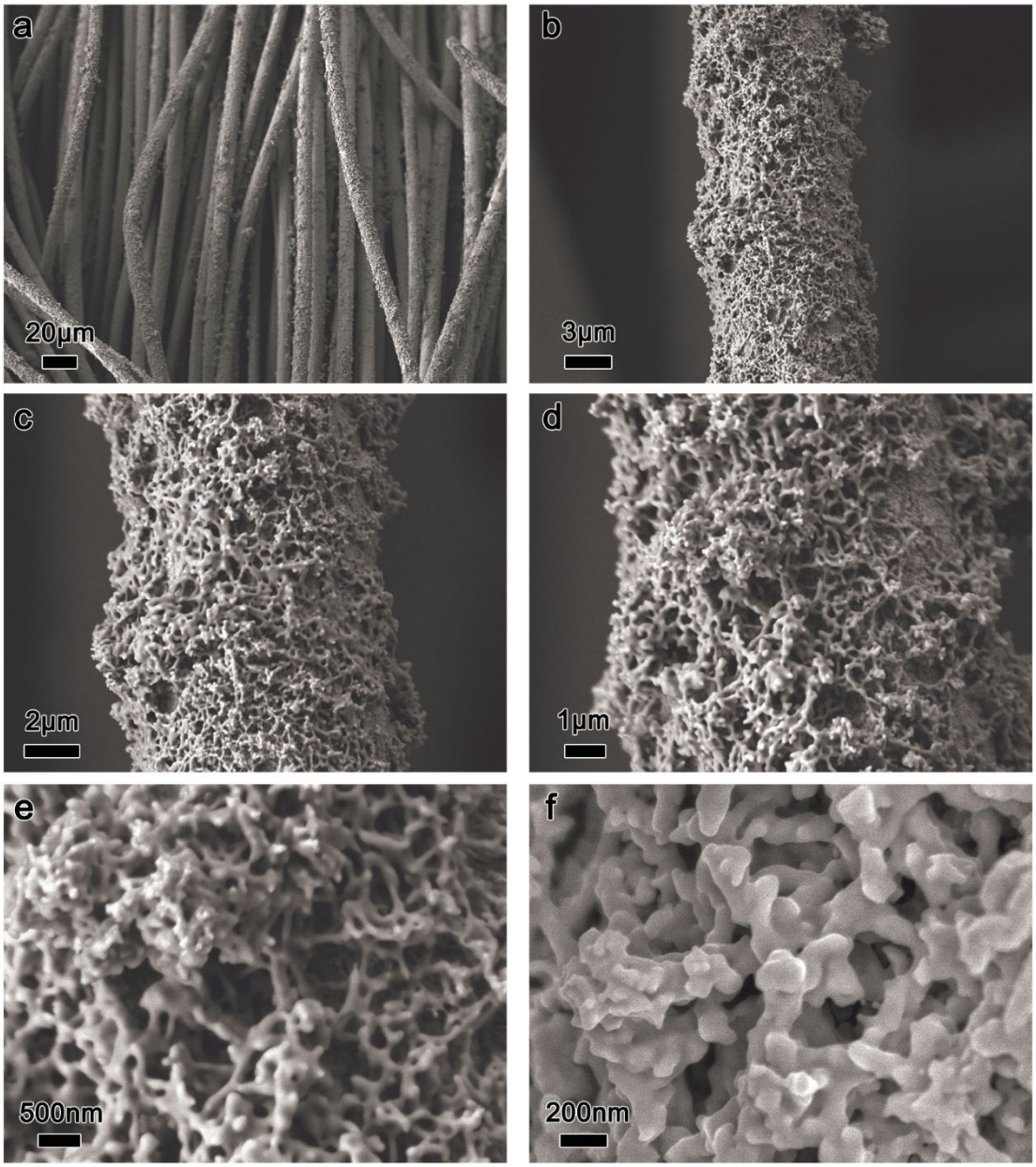

Figure S10. SEM images of the **MIL-SP** (a-f) with different levels of magnification.

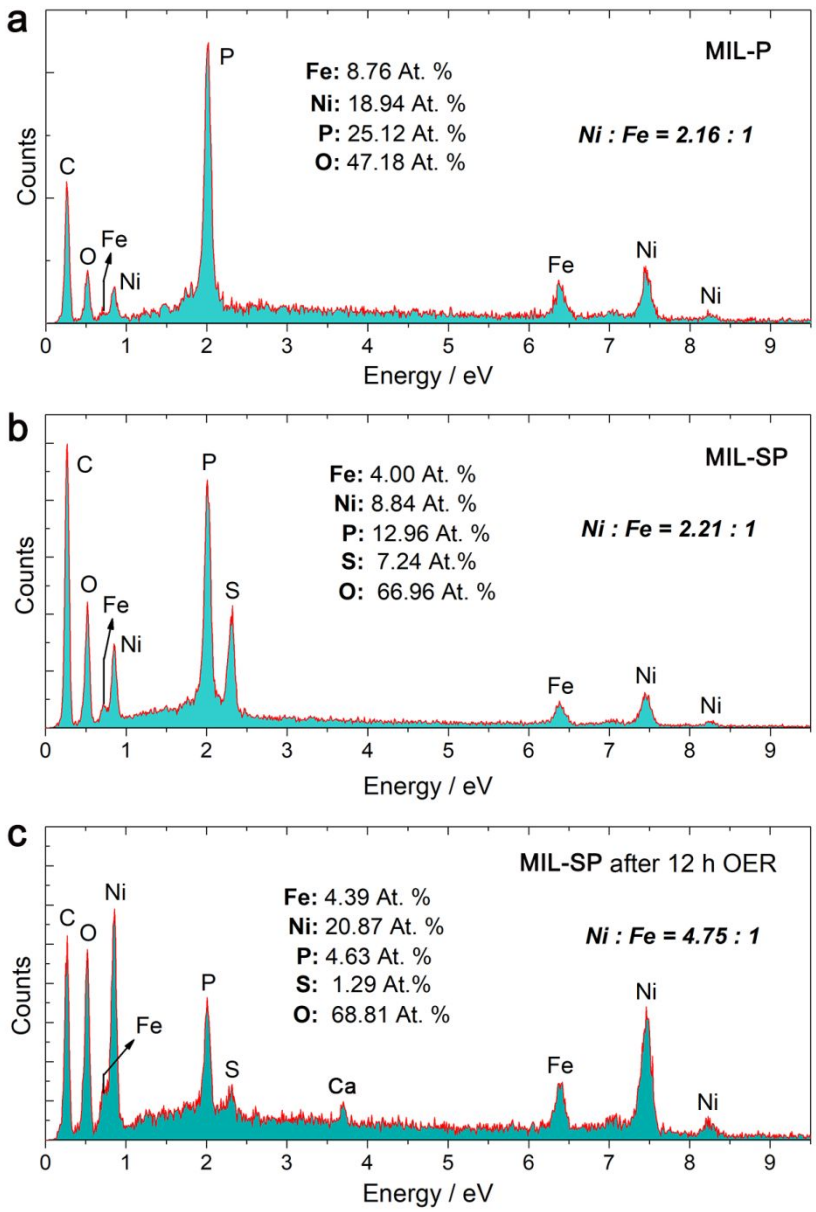

Figure S11. Energy dispersive X-ray (EDX) spectrum of (a) MIL-P, (b) MIL-SP, and (c) MIL-SP after 12 h OER at a constant current density of 50 mA cm^{-2}.

After low-temperature phosphorization treatments, the MIL-P and MIL-SP exhibit a close Ni/Fe atomic ratio to their corresponding MIL-OH and MIL-S precursors, respectively (**Figure S8**). The high atomic percentage of P in MIL-P indicates the successful introduction of P ligands into the MIL-OH precursors, possibly due to the formation of metal phosphide or phosphate. Meanwhile, EDX spectrum of MIL-SP reveals the presence of both S and P ligands, which implies the probable formation of metal phosphosulphides. The relatively high atomic percentage of O element in MIL-SP indicates the existence of phosphorous oxides, physically-absorbed H_2O, and certain metal oxide species, as supported by the following XPS data (**Figure S21**). After OER at 50 mA cm^{-2} for 12 hours, the atomic percentages of P and S elements in MIL-SP obviously decreased, due to the oxidation of surface-residing P and S ligands upon OER. Moreover, after this long-time OER, the Ni/Fe atomic ratio of MIL-SP increased to 4.75 :1 from initial 2.21:1, implying the loss of Fe species during the OER. Remarkably, during long-time O_2-evolved catalysis, the loss of Fe species from highly active $NiFeO_x$-based OER electrocatalysts into electrolytes was also previously observed, which was considered to be one key reason for the gradual deactivation of $NiFeO_x$-based OER electrocatalysts with time.[15]

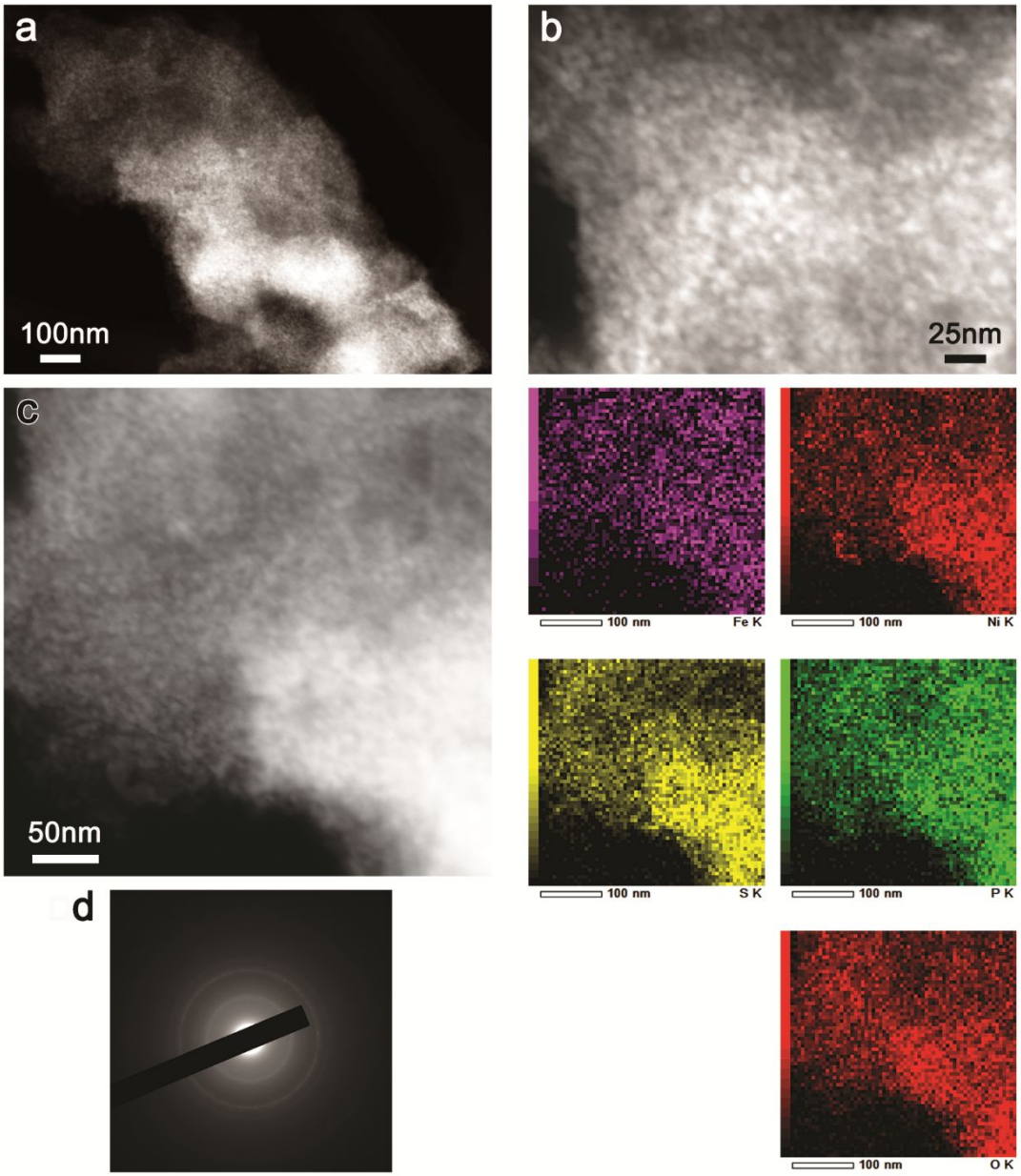

Figure S12. (a-c) High angel dark-field scanning transmission electron microscopy images (HADR- STEM) of the MIL-SP, and the corresponding EDX elemental mapping images of the area in (c). (d) Selected area electron diffraction (SAED) patterns of the area in (c).

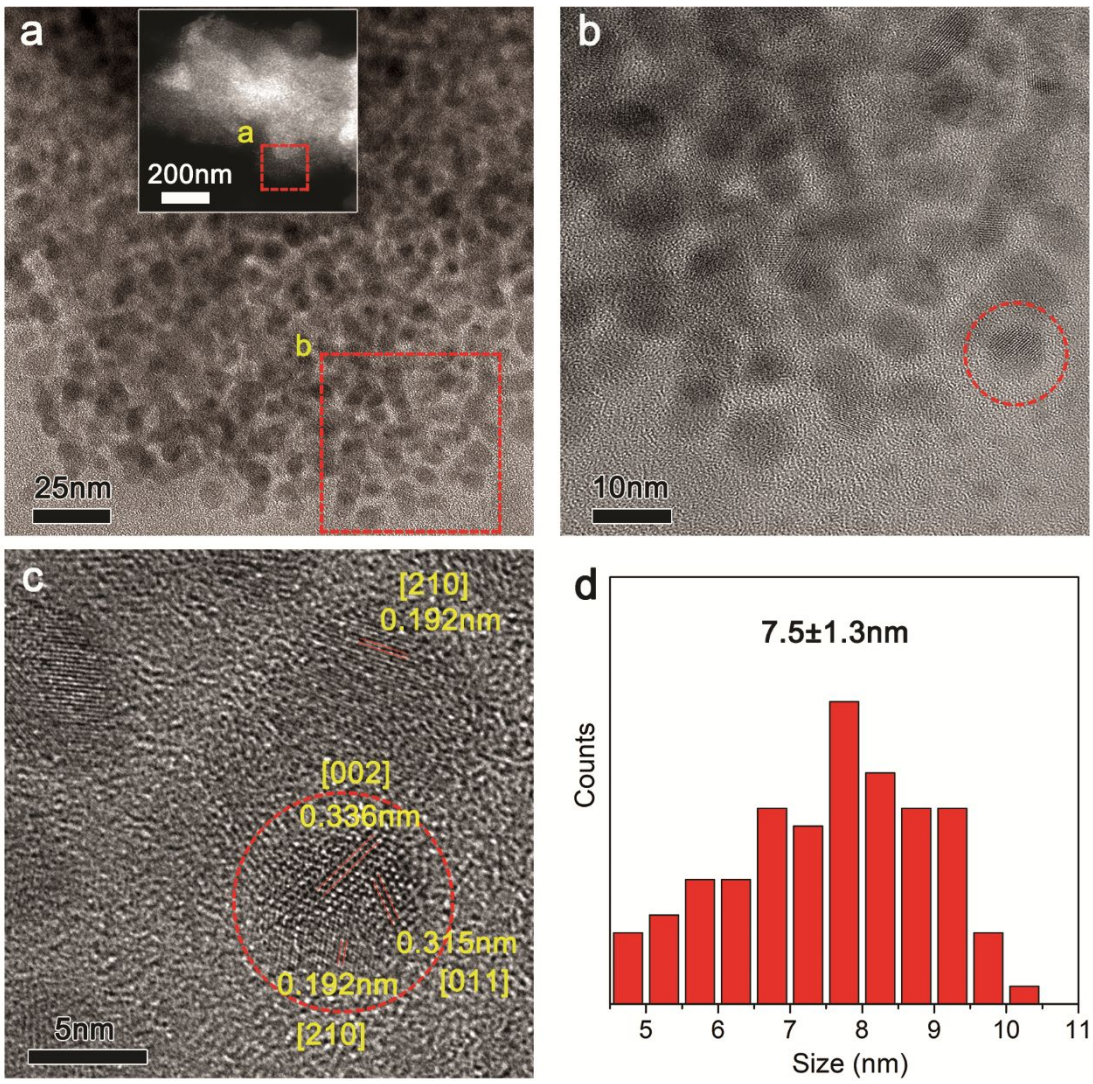

Figure S13. (a) Transmission electron microscopy (TEM) image of MIL-SP from the selected area in the inset; Inset show the HADR-STEM image of MIL-SP. (b-c) High-regulation TEM (HR-TEM) images of MIL-SP from a selected area in (a). (d) Size distribution of the nanoparticles in (a), calculated from random 100 particles.

The HR-TEM image in **Figure S13c** confirms that the nanoparticles in MIL-SP have a crystalline structure. However, due to the complex element compositions, all the crystalline lattices of MIL-SP can't be indexed to one special crystalline structure. Here, the lattice d-spacing value of 0.192 nm well matches with the lattice fringes of [210] plane of Fe_2P (PDF#27-1171) or Ni_2P (PDF#03-0953). In view of the Fe/Ni ratio (~1:2) in the MIL-SP, this lattice d-spacing value might belong to a Fe-doping Ni_2P structure. Meanwhile, the lattice d-spacing values of 0.336 nm and 0.315 nm is very close to lattice fringes of [002] (0.333 nm) and [011] (0.313 nm) planes in the Allabogdanite lattice structure of $(Fe, Ni)_2P$ (PDF#51-1126), except for a slight deviation, which should be attributed to the doping of S element and/or the varying Fe/Ni ratio.

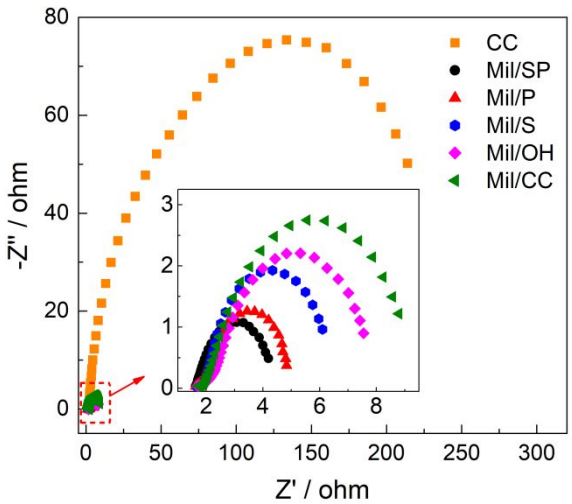

Figure S14. Nyquist plots of the samples recorded at 1.475 V vs RHE.

The Nyquist plots of the carbon cloth supports (CC) and the catalysts show an apparent semicircle in the high-frequency range, which is related to charge transfer resistance (R_{ct}) upon OER. The MIL-SP featured the smallest semicircle diameter and thus the smallest R_{ct}.

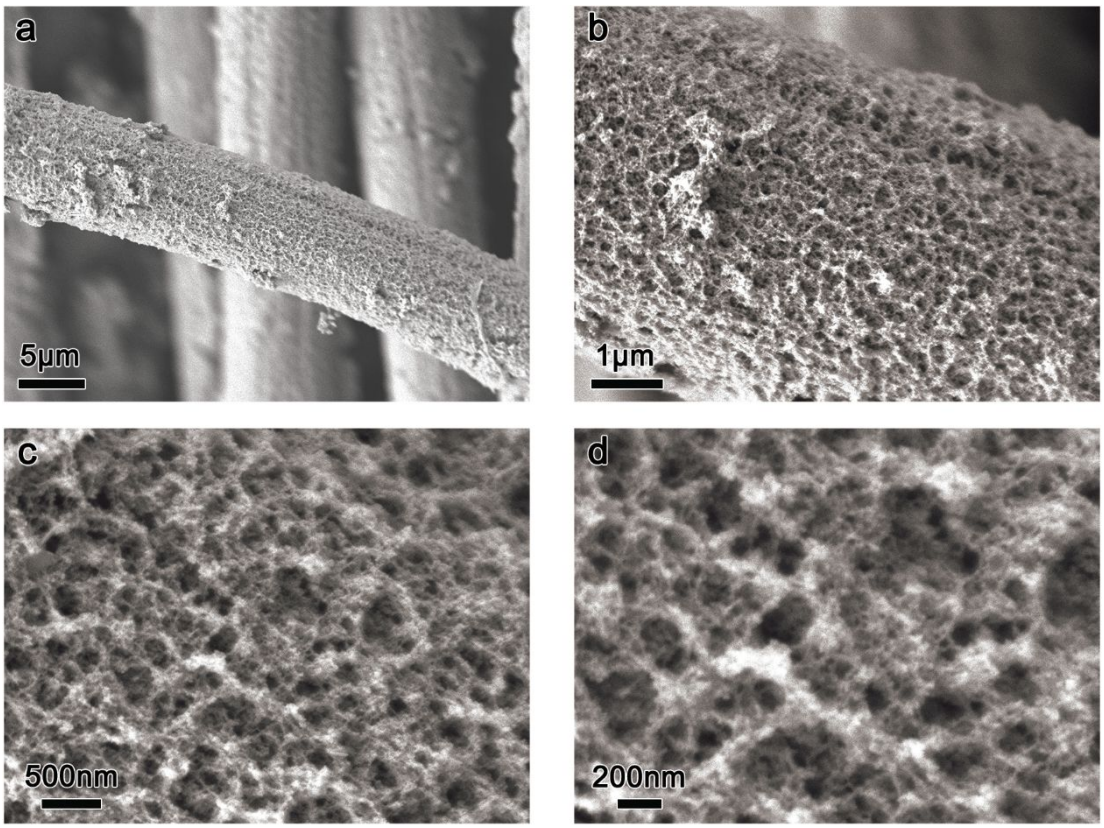

Figure S15. SEM images of the MIL-SP (a-d) after continued OER tests at a constant current density (50 mA/cm^2) for 12 hours.

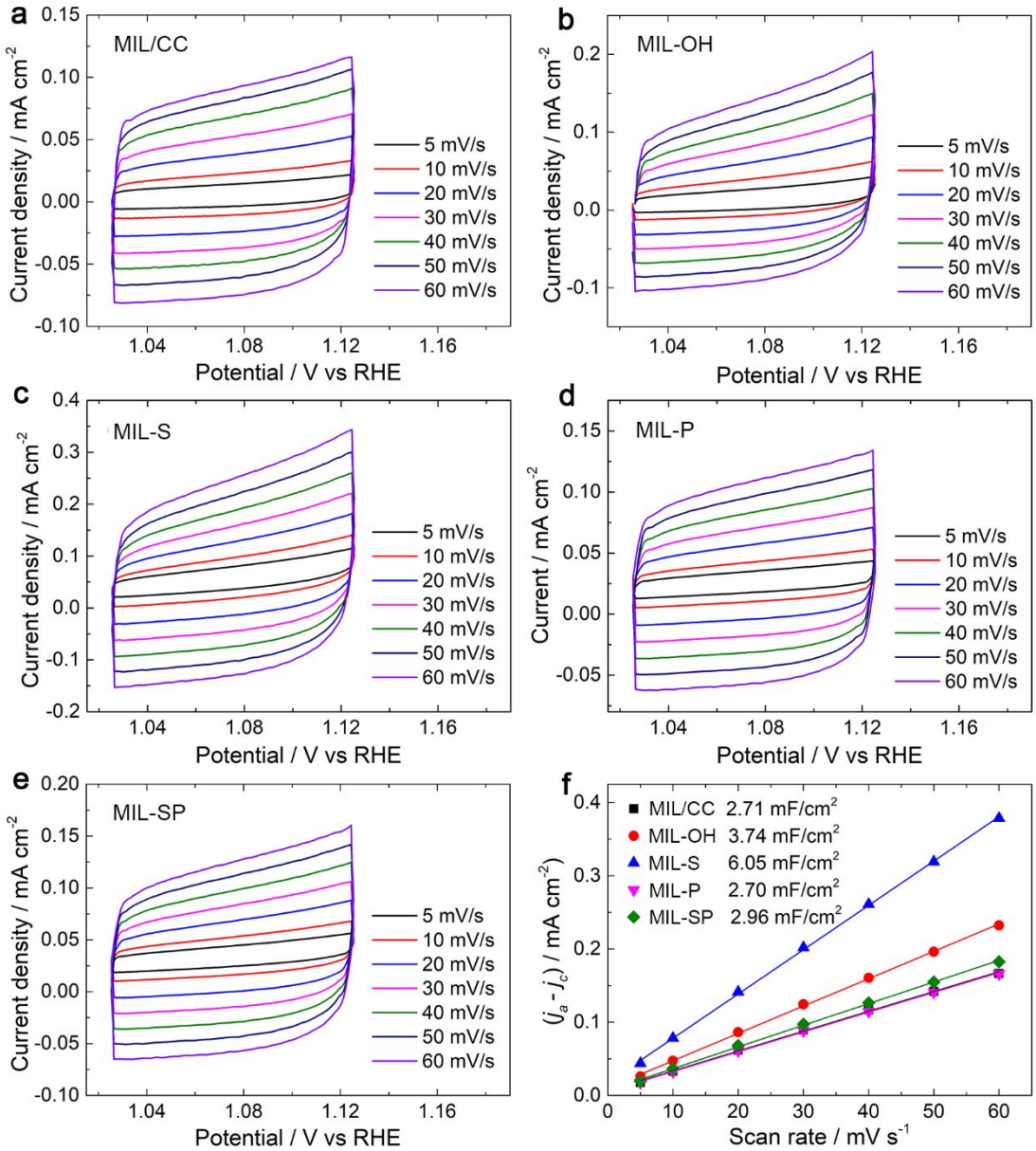

Figure S16. (a-e) Cyclic voltammograms (CVs) of the samples measured at different scan rates from 5 to 60 mV s^{-1}. (f) Plots of the charge current density differences ($\Delta j = j_a - j_c$) at 1.0754 V_{RHE} vs. the scan rates (the slope of the plots is associated with the electrochemical double-layer capacitance per geometric area of electrode).

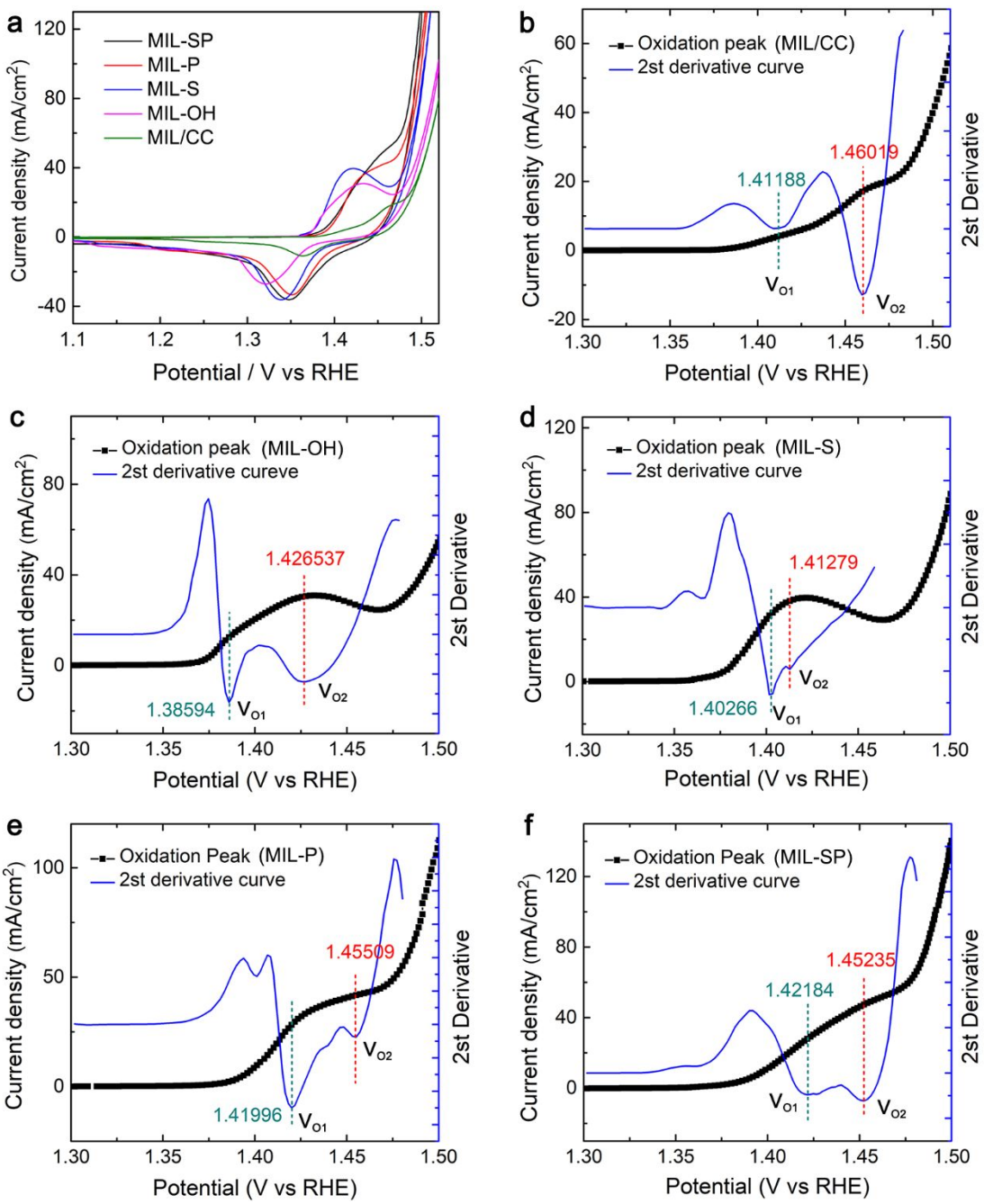

Figure S17. (a) Cyclic voltammograms (CV) tests of the samples for OER at a scan rate of 10 mV s^{-1}. (b-f) Second derivative curves of the anodic current part of the CV curves, which are employed to identify the peak positions of oxidation current of Ni^{2+}/Ni^{3+}.

Obviously, all the samples show two oxidation peaks of Ni^{2+}/Ni^{3+}, indicating that Ni^{2+} reside in two different coordination environments. Considering the Raman spectra of the samples (**Figure S4 and Figure S5**), the more positive oxidation peak (V_{O2}, at 1.41-1.47 V_{RHE}) of Ni^{2+}/Ni^{3+} should be from a Fe^{3+}-X-Ni^{2+} motif, while the relatively negative oxidation peak (V_{O1} at 1.38-1.42 V_{RHE}) should be from a Ni^{2+}-X-Ni^{2+} motif (X = O, P, S, and BDC ligands). The differences of the V_{O1} and V_{O2} between the samples should be due to their different anionic ligands, as discussed in the following XPS data.

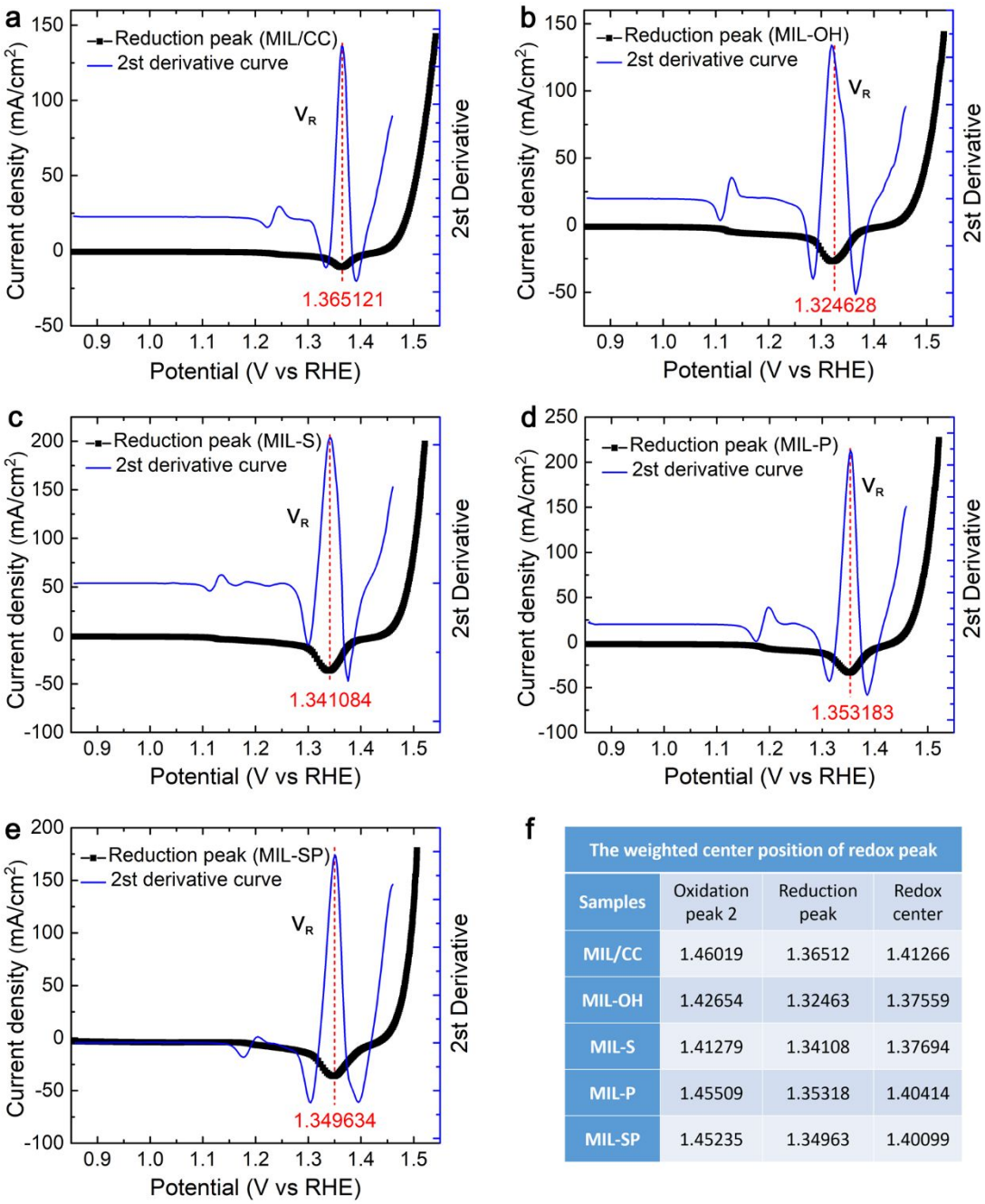

f

The weighted center position of redox peak			
Samples	Oxidation peak 2	Reduction peak	Redox center
MIL/CC	1.46019	1.36512	1.41266
MIL-OH	1.42654	1.32463	1.37559
MIL-S	1.41279	1.34108	1.37694
MIL-P	1.45509	1.35318	1.40414
MIL-SP	1.45235	1.34963	1.40099

Figure S18. (a-e) Second derivative curves of the cathodic current part of the CV curves, which are employed to identify the peak positions of reduction current of Ni^{2+}/Ni^{3+}. (f) The calculation of the redox weighted center position of Ni^{2+}/Ni^{3+}.

Nearly all the samples show only one reduction peak (V_R) of Ni^{2+}/Ni^{3+}, but different sample exhibits a different reduction peak potential, which provides a view for understanding the OER processes, as discussed in **Figure S23**. The redox weighted center position is the average value of the V_{O2} (**Figure S17**) and V_R.

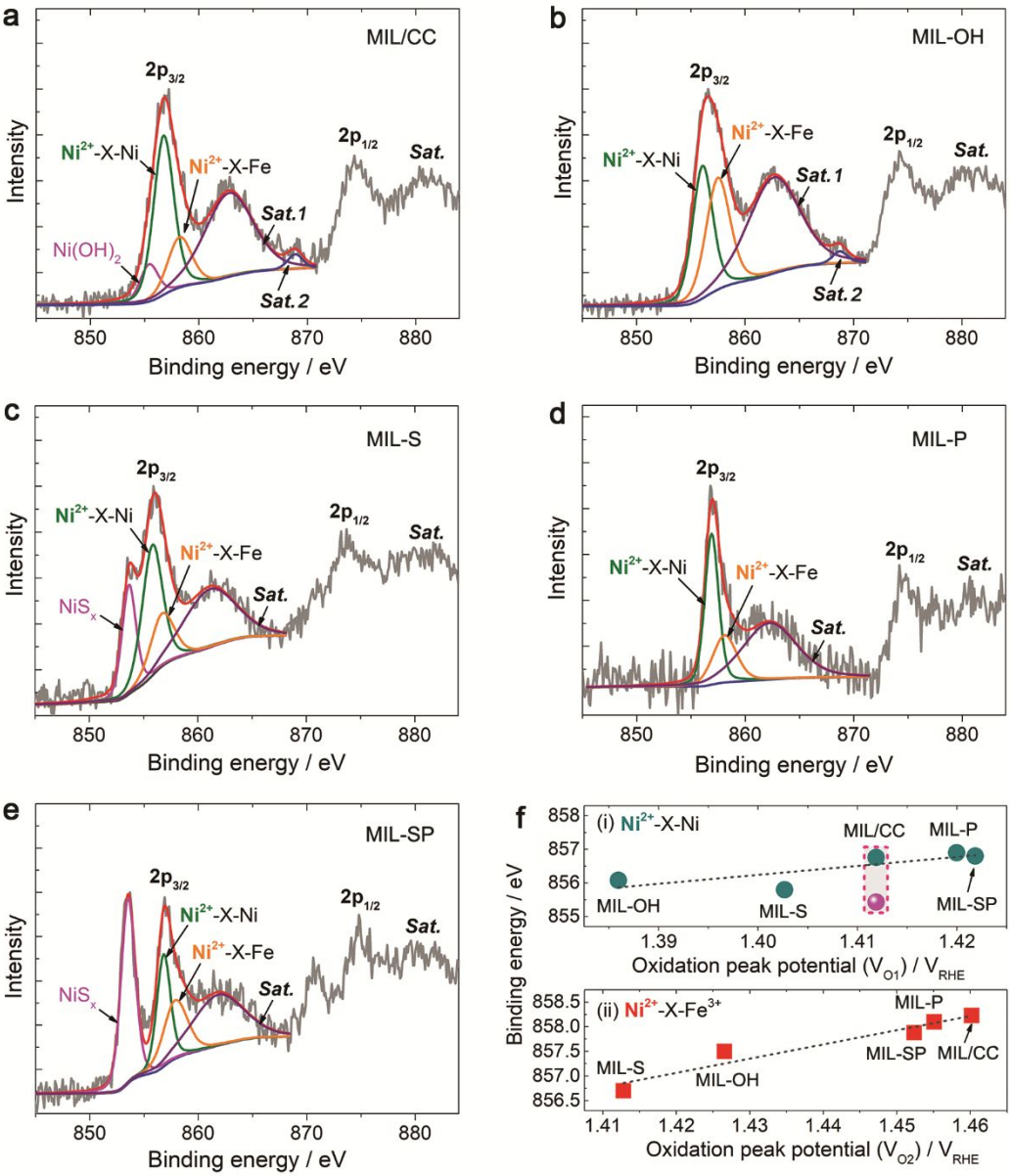

Figure S19. (a-e) Ni 2p XPS core-level spectra of the as-prepared samples and corresponding fitted peaks of the Ni $2p_{3/2}$ part. The fitted peak parameters were summarized in **Table S2**. (f) The relationships between the binding energy (BE) of Ni^{2+} component peaks and the oxidation peak potentials ((i) V_{O1} and (ii) V_{O2}) of Ni^{2+}/Ni^{3+} in **Figure S17**.

In **Figure S19**, the Ni $2p_{3/2}$ XPS spectrum of the samples can be mainly fitted into three peaks, except for that of MIL/CC, MIL-S, and MIL-SP with a shoulder peak at a lower BE.

For MIL/CC, the shoulder peak at 855.42 eV is assigned to Ni^{2+} of $Ni(OH)_2/NiO_x$ formed during the EPD process,[16,17] while the main peak at about 556.9 eV (close to 557.2 eV in MIL-53 powder in **Figure S22**) can be assigned to Ni^{2+} species in the MIL-53 frameworks.[18] The higher BE of Ni^{2+} in the MIL-53 frameworks than that of Ni^{2+} in pure $Ni(OH)_2$ is because of the strong electron-withdrawing ability of BDC ligands and the Fe^{3+} dopants. Considering the Raman spectra of MIL/CC and MIL-53 powder (**Figure S4**), the Ni^{2+} species in the MIL-53 frameworks can be further deconvoluted into two peaks at 856.78 eV and 858.23 eV, which correspond to two different Ni^{2+} coordination conditions (Ni^{2+}-X-Ni and Ni^{2+}-X-Fe, X = O, or BDC), respectively. The presence of $Ni(OH)_2/NiO_x$ component in MIL/CC is further supported by the small satellite peak (***Sat. 2***) at 868.88 eV, which is a characteristic signal of $Ni(OH)_2$.[17,19,20] The left peak at 862.76 eV is owing to the Ni satellite peak.[20] Moreover, comparison of Ni $2p_{3/2}$ XPS spectrum between MIL/CC and MIL-53 powder was given **Figure S22**.

For MIL-OH, the characteristic signal of $Ni(OH)_2$ (***Sat. 2***, at 868.73 eV) can be also observed.[19-21] As such, in combination with the Raman results (**Figure S4**) and CV curves (**Figure S17**), the peaks located at 856.08 eV and 857.5 eV can be assigned to Ni^{2+} in the Ni^{2+}-O-Ni ($Ni(OH)_2$/NiO phase) and Ni^{2+}-O-Fe ($NiFe_2O_4$ phase) motifs, respectively. The left peak at 862.63 eV is from the Ni satellite peak.

In MIL-S, the shoulder peak at 853.65 eV is owing to the Ni^{2+} species in NiS_x phase.[22] This result suggests the formation of metal sulfides during the EC-MOF process. The adjacent two peaks at 855.8 eV and 856.7 eV should be from partly-oxidized (in air) metal sulfides in Ni^{2+}-X-Ni and Ni^{2+}-X-Fe (X = O or S) motifs, respectively. The lower BE of these two peaks than that of MIL-OH should be ascribe to the electron-denoting nature of S ligands in the partly-oxidized metal sulfides. Hence, there should be both Metal-S (M-O) and Metal-O (M-O) bonds on the partly oxidized surface of MIL-S. The peak at 861.11 eV is owing to the Ni satellite peak.

For MIL-P, there is no XPS component peak related to the NiP_x, which may be due to the easier oxidation of NiP_x exposed to air. The P 2p XPS spectrum in **Figure S22c** further reveals the surface oxidation of MIL-P, with a strong signal of PO_x. Besides, depth-profiling Ni 2p XPS measurements of MIL-P after 300s Ar^+ etching show the existence of NiP_x (**Figure S28e**). Thus, in **Figure S19d**, the two peaks at 856.9 eV and 858.1 eV can be derived from the partly-oxidized metal phosphides and correspond to Ni^{2+}-X-Ni and Ni^{2+}-X-Fe (X = O or P) motifs, respectively. The higher BE of Ni^{2+} component peaks in MIL-P than that of MIL-OH indicate the stronger electron-withdrawing ability of P ligands than that of O ligands. Thus, there are also M-O and M-P bonds in the MIL-P. The left peak at 862.22 eV is from the Ni satellite peak.

In MIL-SP, the low BE peak at 853.53 eV is attributed to the $Ni^{\delta+}$ ($0 < \delta < 1$) sites on $NiSP_x$.[23] As compared to MIL-P and MIL-SP, the MIL-SP show a much stronger XPS signal of the metallic component ($NiSP_x$), suggesting the higher anti-oxidation stability of $NiSP_x$ in air. This deduction is also supported by the Raman spectra of MIL-SP after OER tests (**Figure S5**). In **Figure S19e**, the peaks at 856.8 eV and 857.88 eV should correspond to the Ni^{2+} of partly-oxidized metal phosphosulphide in Ni^{2+}-X-Ni and Ni^{2+}-X-Fe (X = O, S, or P) motifs, respectively. The two Ni^{2+} components in MIL-SP have a BE value between those of Ni^{2+} in MIL-S and MIL-P, implying the synergistic effects of S and P ligands in tuning the electron structure of Ni^{2+} centers. Finally, the peak at 861.82 is from the Ni satellite peak.

Considering the redox behavior of Ni^{2+}/Ni^{3+} couple in **Figure S17**, the oxidation peak potential of Ni^{2+}/Ni^{3+} directly corresponds to the energy required for electron loss from Ni^{2+} sites to electrode surface, thus indirectly reflecting the electron density of Ni^{2+} center in the samples. This is, the more positive oxidation peak potential of the samples, the lower electron density (or the higher XPS BE) of their Ni^{2+} centers. Within this context, the relationships between the oxidation peak potential (Ni^{2+}/Ni^{3+}) and the BE of Ni^{2+} $2p^{3/2}$ component peaks were built. As shown in **Figure S19f**, as increasing the oxidation peak potential of the samples, their BE of Ni^{2+} $2p^{3/2}$ component peaks linearly increase. This result suggests that the Ni $2p^{3/2}$ XPS fitted peaks well reveal the coordination environments of Ni^{2+} sites in the as-prepared samples.

In the **Figure S19f (i)**, the pink point of MIL/CC at a lower BE is from the $Ni(OH)_2/NiO_x$ formed during EPD. Besides, the V_{O1} of MIL-S is more positive than that of MIL-OH, although the Ni^{2+} in MIL-S shows a lower BE. The same condition happens to the MIL-SP and MIL-P. This phenomenon might be attributed be the varying degrees of cooperation between the interconnected Ni^{2+}-X-Ni^{2+} and Ni^{2+}-X-Fe^{3+} phases, induced by the ligands. This deduction can be supported by the differences between V_{O1} and V_{O2} of different samples (**Figure S17**). As shown in **Figure S17**, the oxidation peak difference of MIL-S (V_{O2}-V_{O1} = 0.01013 V) is obviously smaller than that of MIL-OH (0.040597 V), while the peak difference of MIL-SP (0.03051 V) is smaller than that of MIL-P (0.03513 V). The smaller oxidation peak difference should be stemmed from the enhanced cooperation between the interconnected Ni^{2+}-X-Ni^{2+} and Ni^{2+}-X-Fe^{3+} phases in the samples. Obviously, the introduction of S^{2-}

ligands (MIL-S and MIL-SP) helps to improve the cooperation between the interconnected Ni^{2+}-X-Ni^{2+} and Ni^{2+}-X-Fe^{3+} phases. This unique role of S^{2-} ligands should be due to its electron-donating nature, which helps to improve the conductivity of the catalysts matrix and thus electron exchange between the Ni^{2+}-X-Ni^{2+} and Ni^{2+}-X-Fe^{3+} phases. Indeed, it has been well documented that metal sulfides commonly show a higher conductivity than their metal oxide counterparts.[28]

Thus, electron-donating S^{2-} ligands exhibit two important roles: 1) giving electrons to bonded metal ions, leading to lower BE of Ni^{2+} in MIL-S and MIL-SP than that in MIL-OH and MIL-P, respectively; 2) improving the conductivity and thus electron exchange between the Ni^{2+}-X-Ni^{2+} and Ni^{2+}-X-Fe^{3+} phases, leading to positive shift of the V_{O1} peak but negative shift of V_{O2} peak for MIL-S and MIL-SP, as shown in Figure S19f.

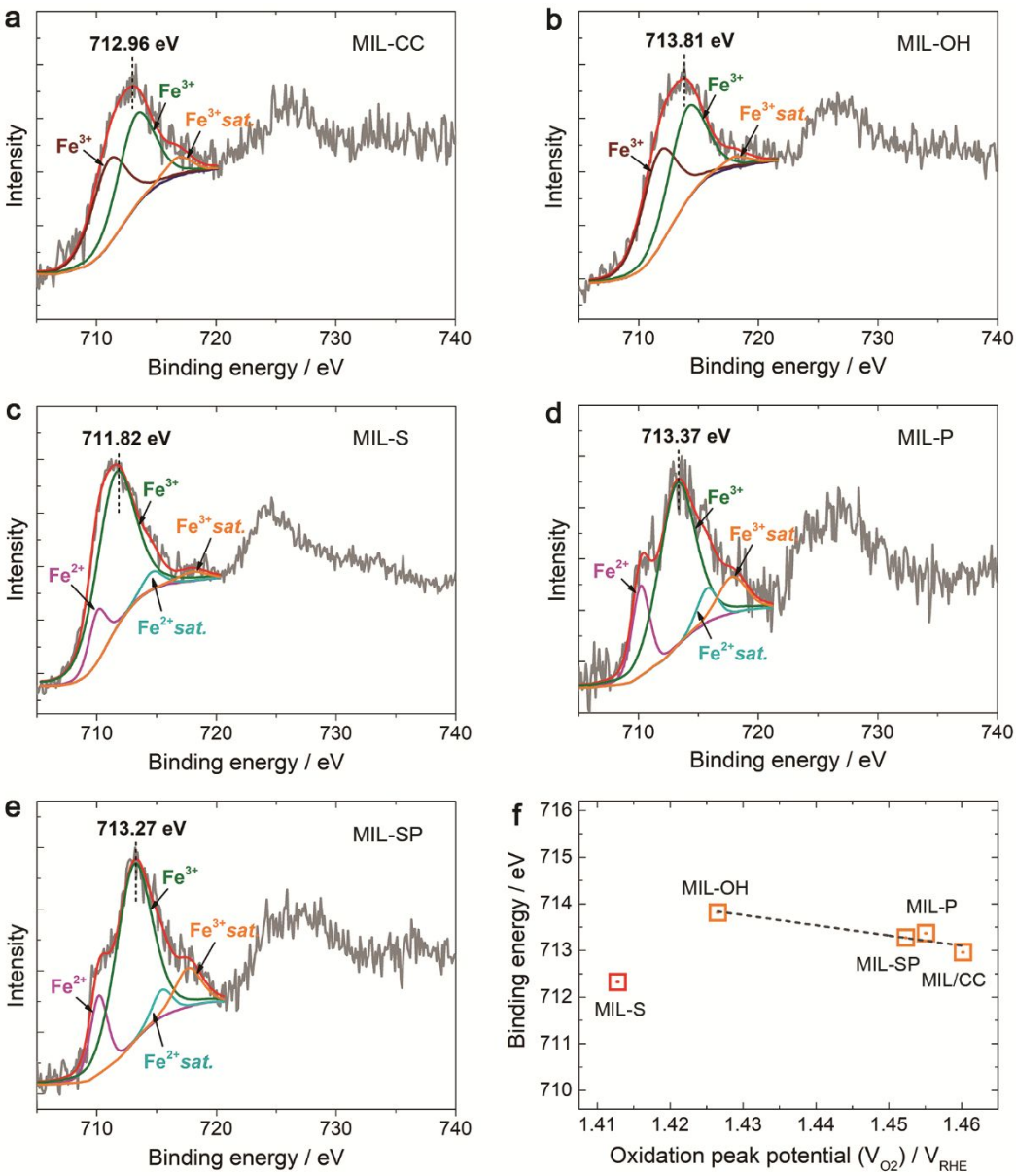

Figure S20. (a-e) Fe 2p XPS core-level spectra of the as-prepared samples and corresponding fitted peaks of the Fe $2p_{3/2}$ part. The fitted peak parameters were summarized in **Table S3**. (f) The relationships between the binding energy (BE) of Fe^{3+} component peaks and the oxidation peak potentials (V_{O2}) of Ni^{2+}/Ni^{3+} in **Figure S17**.

In MIL-CC and MIL-OH, the Fe $2p_{3/2}$ XPS spectra was fitted into two Fe^{3+} component peaks (BE > 711.0 eV) and one Fe^{3+} satellite peak (BE = ~716-718 eV).[23-28] In contrast, there is a Fe^{2+} shoulder peak (BE = ~710 eV) in the Fe $2p_{3/2}$ XPS spectra of MIL-S, MIL-P, and MIL-SP, which should be from the gradually oxidation of metal sulfides,[28] metal phosphides,[24,25] and metal phosphosulphide,[23] respectively. Besides, the three samples have one Fe^{3+} component peaks and two satellite peaks corresponding to Fe^{2+} and Fe^{3+}. All the fitted peak parameters were shown in **Table S3**. To compare the BE differences of Fe^{3+} components of the samples (**Figure S20f**), the peak position of the sum fitted cure in MIL/CC (**Figure S20a**) and MIL-OH (**Figure S20b**) were chosen to represent the Fe^{3+} BE in their Ni^{2+}-X-Fe^{3+} motif, because it is difficult to identify which of the two Fe^{3+} components has a higher contribution in their Ni^{2+}-X-Fe^{3+} motif.

Considering the inductive effects between Fe^{3+} and Ni^{2+} in the Ni^{2+}-X-Fe^{3+} motif of the samples, the relationships between Fe^{3+} BE and the oxidation peak potential (V_{O2}) of Ni^{2+}/Ni^{3+} were built. As shown in **Figure S20f**, except for MIL-S, the Fe^{3+} BE of the samples linearly deceases as positive shift of their V_{O2}. The decrease of Fe^{3+} BE corresponds to the increasing electron density of the Fe^{3+} centers, while the positive shift of V_{O2} suggests the decreasing electron density of the Ni^{2+} centers. Hence, the electron transfer efficiency from Ni^{2+} to Fe^{3+} is improved in an increasing order from O, P, and BDC. Obviously, electron-withdrawing ligands tend to enhance the inductive effects between Fe and Ni sites. In contrast, as electron-denoting ligands, the S ligands decrease the BE of both Fe^{3+} and Ni^{2+} (**Figure S19f**) centers and thus weaken the inductive effect between them.

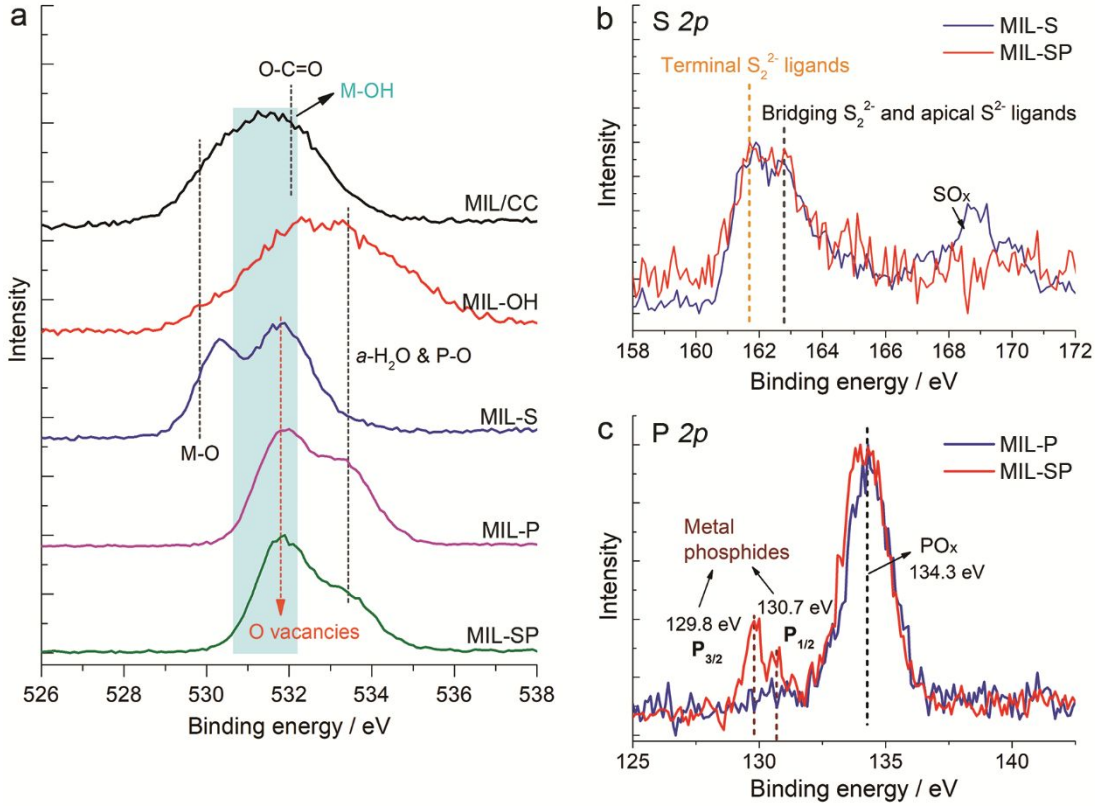

Figure S21. (a) High-regulation O 1s XPS spectra of the as-prepared samples, (b) S 2p XPS spectra of MIL-S and MIL-SP. (c) P 2p XPS spectra of MIL-P and MIL-SP.

In **Figure S21a**, O 1s XPS reveals the presence of Metal-O (M-O at ~530 eV) bonds of metal oxide phase in MIL/CC, MIL-

OH, and MIL-S.[16] This result indicates the surface oxidation of MIL-S, due the breaking of M-S bonds, as further proved by the S 2p XPS spectra of MIL-S (b).[3] Thus, in MIL-S, there are both M-O and M-S bonds, well consistent with its Ni and Fe $2p_{3/2}$ spectra. For MIL-P and MIL-SP, the bulk metal oxide phase can be ignored and there is a high percentage of P-O bonds (PO_x),[25,29] in accordance with their P 2p XPS spectra (c). Interestingly, there is a similar O 1s XPS peak at ~531.6 eV in MIL-S, MIL-P and MIL-SP, which was suggested to be defect sites with a low oxygen coordination (O vacancies).[30] These O vacancies could facilitate the OER over their adjacent metal sites. Certainly, there should be M-O bonds (O with a low oxygen coordination) in MIL-P and MIL-SP. Thus, the P ligand may exist in the forms of O-M-P and M-PO_x species.[29] In **Figure S21c**, the higher content of metal phosphides phase (129.8 eV and 130.7 eV)[24] in MIL-SP than that in MIL-P suggests the higher anti-oxidation ability of MIL-SP in air.

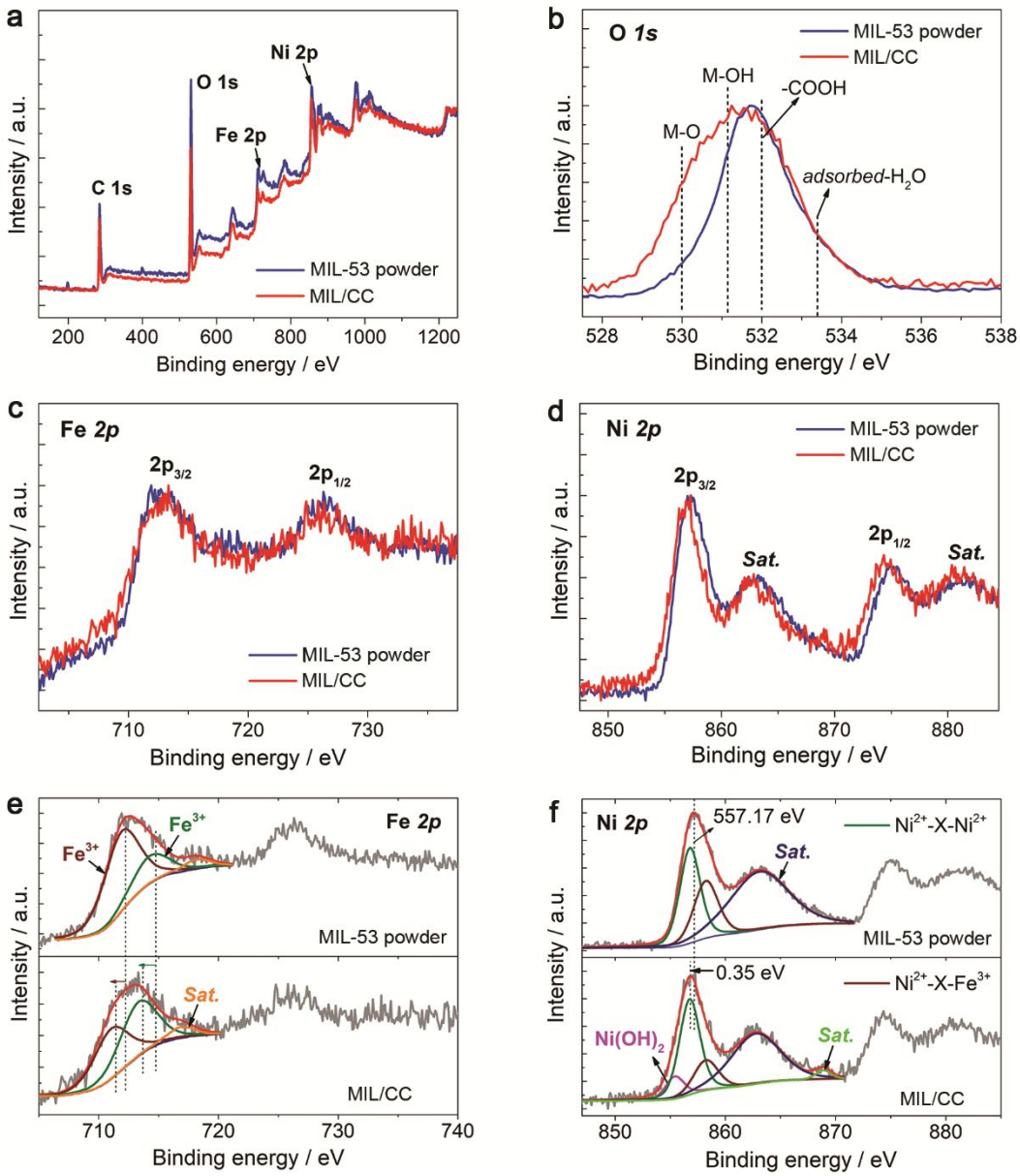

Figure S22. (a) XPS survey spectra of MIL-53 powder and MIL/CC. (b-d) Comparison of the O 1s, Fe 2p, and Ni 2p XPS spectra between MIL-53 power and MIL/CC. (e) Comparison of the Fe $2p_{3/2}$ fitted peaks between MIL-53 power and MIL/CC. (f) Comparison of the Ni $2p_{3/2}$ fitted peaks between MIL-53 and MIL/CC.

Notably, O 1s XPS proves the formation of metal oxides and hydroxides ($Ni(OH)_2/NiO_x$) in MIL/CC during the electrophoresis deposition of MIL-53 nanoparticles onto the carbon cloth (CC) supports.[10a,18] Besides, as compared to MIL-53, the Ni and Fe 2p XPS spectra also shift to a litter lower BE area. This results should be due to the lower BE of Ni^{2+} in $Ni(OH)_2/NiO_x$ than that of Ni^{2+} in MIL-53, as discussed above (**Figure S19**), as well as partial hydrolysis of MIL-53 during EPD. [10-12,14-15]

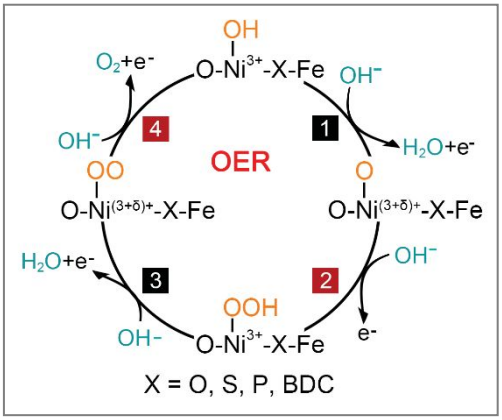

Figure S23. OER process over the Ni^{2+} center linked to Fe^{3+} via different ligands.

Recently, the nature of active sites (Ni *vs.* Fe) in NiFe-based OER catalysts has been heavily debated.[31-34] However, considering the effects of different ligands on the electronic structure and redox behavior of Ni^{2+} and Fe^{3+} sites in our system, the role of ligands in the OER process, which involves a four-electron transfer model with three intermediates (OH*, O*, and OOH*),[35,36] can be well expatiated over Ni^{2+} sites. For the S ligand, the redox of Ni^{2+}/Ni^{3+} turns to be easier (**Step 1 and 3**), as evidenced by the relatively negative oxidation potential but positive reduction potential of MIL-S (**Figure S17** and **Figure S18**). As such, the high valence $Ni^{(3+\delta)+}$ ($1>\delta>0$) in MIL-S possess a relatively weak oxidation ability for extracting electrons from the O intermediates (**Step 2 and 4**). Thus, OER need be driven in a higher overpotential (losing energy). In contrast, for the electron-withdrawing ligands (*e.g.,* P), the oxidation of Ni^{2+} to an active higher valence tends to be more difficult (losing energy) (**Figure 4a** and **Figure S17**), owing to its electron- deficient coordination environments, but the $Ni^{(3+\delta)+}$ ($1>\delta>0$) should have stronger oxidation ability in the subsequent OER step. Obviously, the Ni sites in different coordination environments should have different binding strength towards the reaction intermediates. Accordingly, the best OER activity of MIL-SP should be due to the synergistic effects of S and P ligands, which balance the energy loss of OER (binding strength of the reaction intermediates) when only S or P ligand exists in catalysts. This conclusion is consistent with that of pioneering DFT works by Nørskov et al,[35,36] in which highest OER activity over catalysts is suggested to be achieved at the intermediate binding strength of the reaction intermediates.

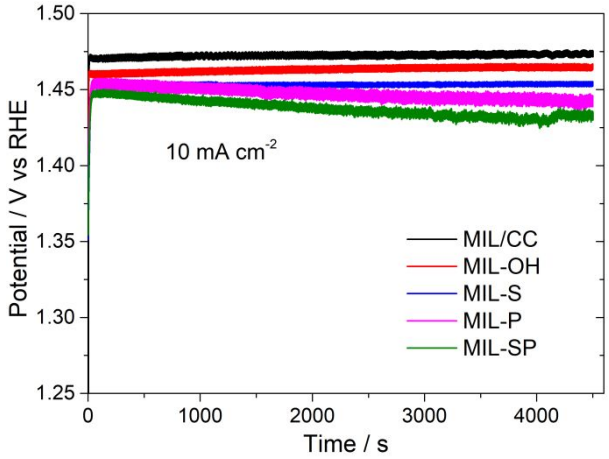

Figure S24. Chronopotentiometry (V-t) curves of the as-prepared samples at a constant current density of 10 mA cm^{-2} for 4500s.

As compared to the stable potential of MIL/CC, MIL-OH and MIL-S, the gradually decreased potential of MIL-P and MIL-SP during the chronopotentiometry test should be attributed to their relatively slower surface oxidation and phase transformation processes, thus leading to the slower formation of active catalytic phase (spinel structure). This conclusion could be derived from the Raman spectra of all the samples before and after OER tests (**Figure S4** and **S5**), as well as the XPS measurements (**Figure S28** and **Figure 29**).

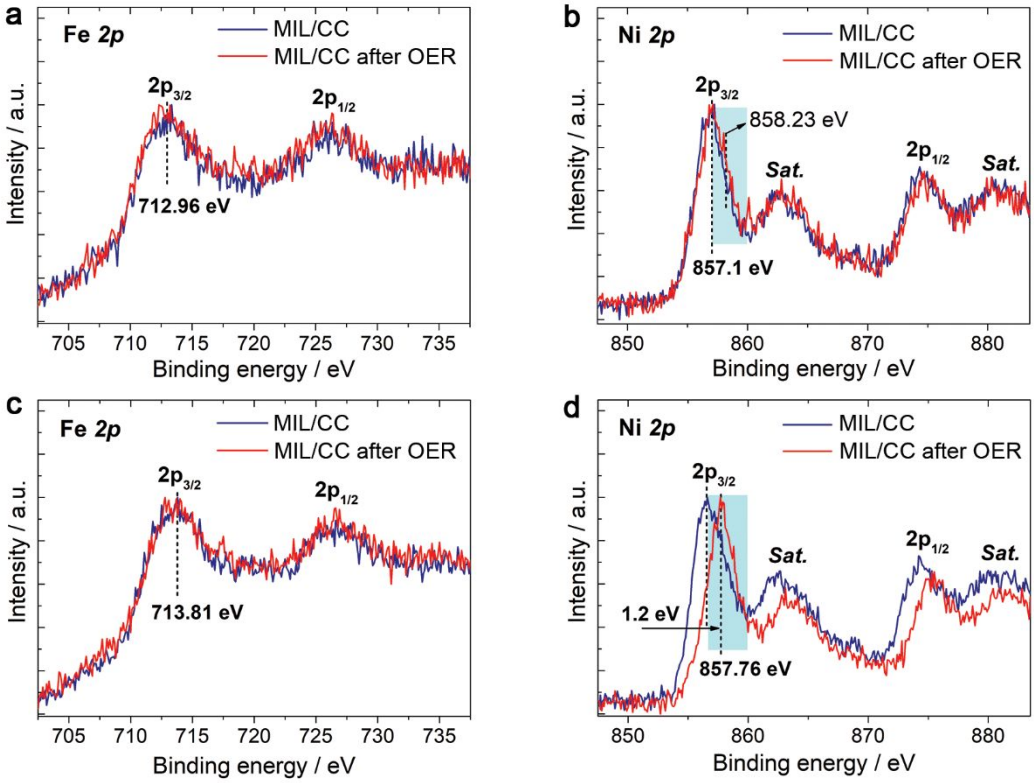

Figure S25. (a, b) Comparison of the Fe 2p and Ni 2p XPS core level spectra of MIL/CC before and after OER tests. (c, d) Comparison of the Fe 2p and Ni 2p XPS core level spectra of MIL-OH before and after OER tests. The OER tests here refer to the Chronopotentiometry measurements in **Figure S22**.

As shown in **Figure S25a** and **S25c**, the Fe 2p XPS spectra of MIL/CC and MIL-OH after OER tests exhibit no obvious difference from that of their original counterparts. Comparatively, the Ni 2p XPS spectra of the samples after OER tests positively shifted to a litter higher binding energy (BE) area. Via a close look at the Ni $2p_{3/2}$ XPS spectra in **Figure S25b** and **S25d**, it can be found that the BE of the marked light blue area is nearly the same as that of Ni^{2+} in the Ni^{2+}-X-Fe^{3+} phase of the MIL/CC and MIL-OH before OER tests (**Table S2**). As such, it can be concluded that the change of Ni $2p_{3/2}$ XPS spectra here is manly attributed to the increasing percentage of Ni^{2+}-X-Fe^{3+} phase (light blue area) after OER tests, which may be from the reconstruction of Fe and Ni sites on the catalysts surface, the diffusion of inner-layer Fe to the surface layer of the catalysts (Seeing the ICP discussions in **Table S1**), as well as the possible adsorption of few Fe^{3+} ion contaminants from the electrolytes.[37]

Nevertheless, the BE of Fe and Ni sites in the Ni^{2+}-X-Fe^{3+} phase basically remains the same, implying that the electronic structure and nature of catalytically-active Fe/Ni sites in MIL/CC and MIL-OH had not been changed after the OER tests (4500s at 10 mA cm^{-2}).

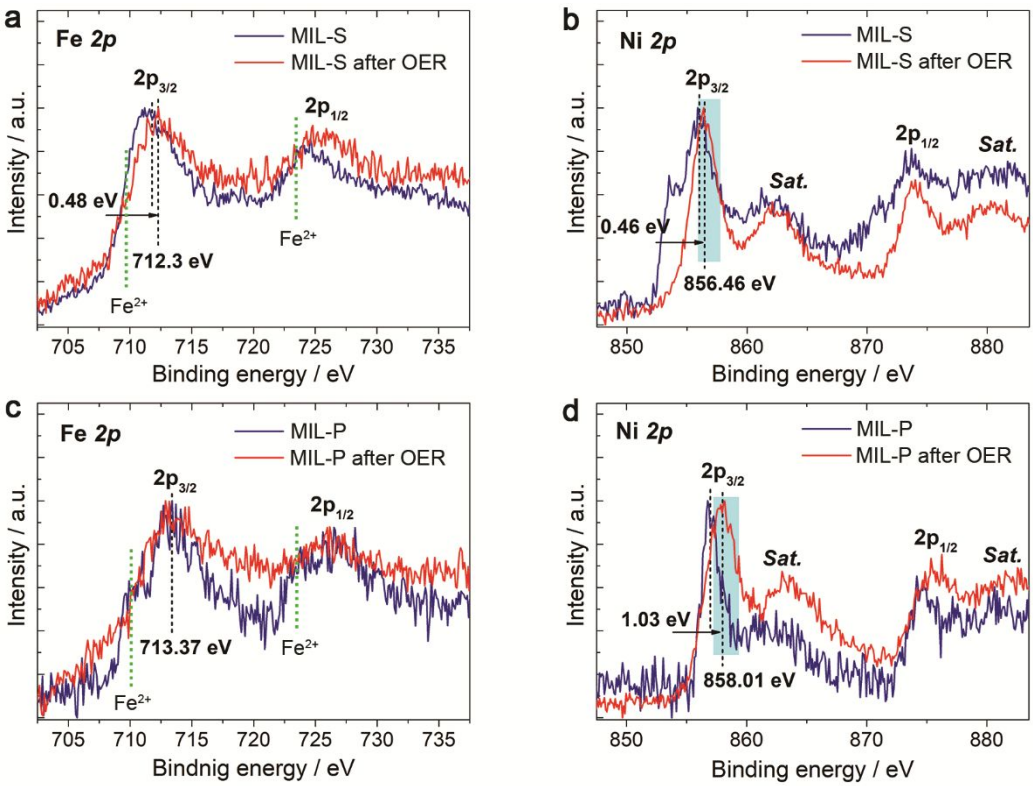

Figure S26. (a, b) Comparison of the Fe 2p and Ni 2p XPS core level spectra of MIL-S before and after OER tests. (c, d) Comparison of the Fe 2p and Ni 2p XPS core level spectra of MIL-P before and after OER tests. The OER tests here refer to the Chronopotentiometry measurements in **Figure S22**.

As shown in **Figure S26a** and **S26c**, the content of reductive Fe^{2+} component in the Fe $2p_{3/2}$ spectra of MIL-S and MIL-P decreases after OER tests. For MIL-S after OER tests (MIL-S-OER), the peak position of Fe $2p_{3/2}$ spectra positively shifts about 0.48 eV, due to the partial oxidation of S ligands upon OER, but it remains at a relatively low BE of ~712.3 eV (**Figure S26a**). This result indicates that the left electron-denoting S ligands can still help to increase the electron density of surface Fe^{3+} centers in the MIL-S-OER. Similarly, although the surface NiS_x component of MIL-S is totally oxidized upon OER (**Figure S26b**), the BE of Ni^{2+} component peak (light blue area) is still close to that of Ni^{2+} (Ni^{2+}-X-Fe motif) in MIL-S before OER (**Table S2**). Therefore, the electronic structures of Fe^{3+}/Ni^{2+} sites in MIL-S didn't have a large change after OER tests.

For MIL-P, the peak position of Fe $2p_{3/2}$ spectra is basically kept at 713.37 eV before and after OER, while the Ni $2p_{3/2}$ spectra shift to a higher BE area. Similar to the Ni $2p_{3/2}$ spectra of MIL-OH after OER (**Figure S25d**), the positive shift of Ni $2p_{3/2}$ spectra of MIL-P after OER is associated with the increasing content of Ni^{2+} in Ni^{2+}-X-Fe^{3+}phase (light blue area in **Figure S26d**). Hence, the nature of Fe/Ni sties in active Ni^{2+}-X-Fe^{3+}phase of MIL-P has no notable change after the oxidation of partial P ligands upon OER.

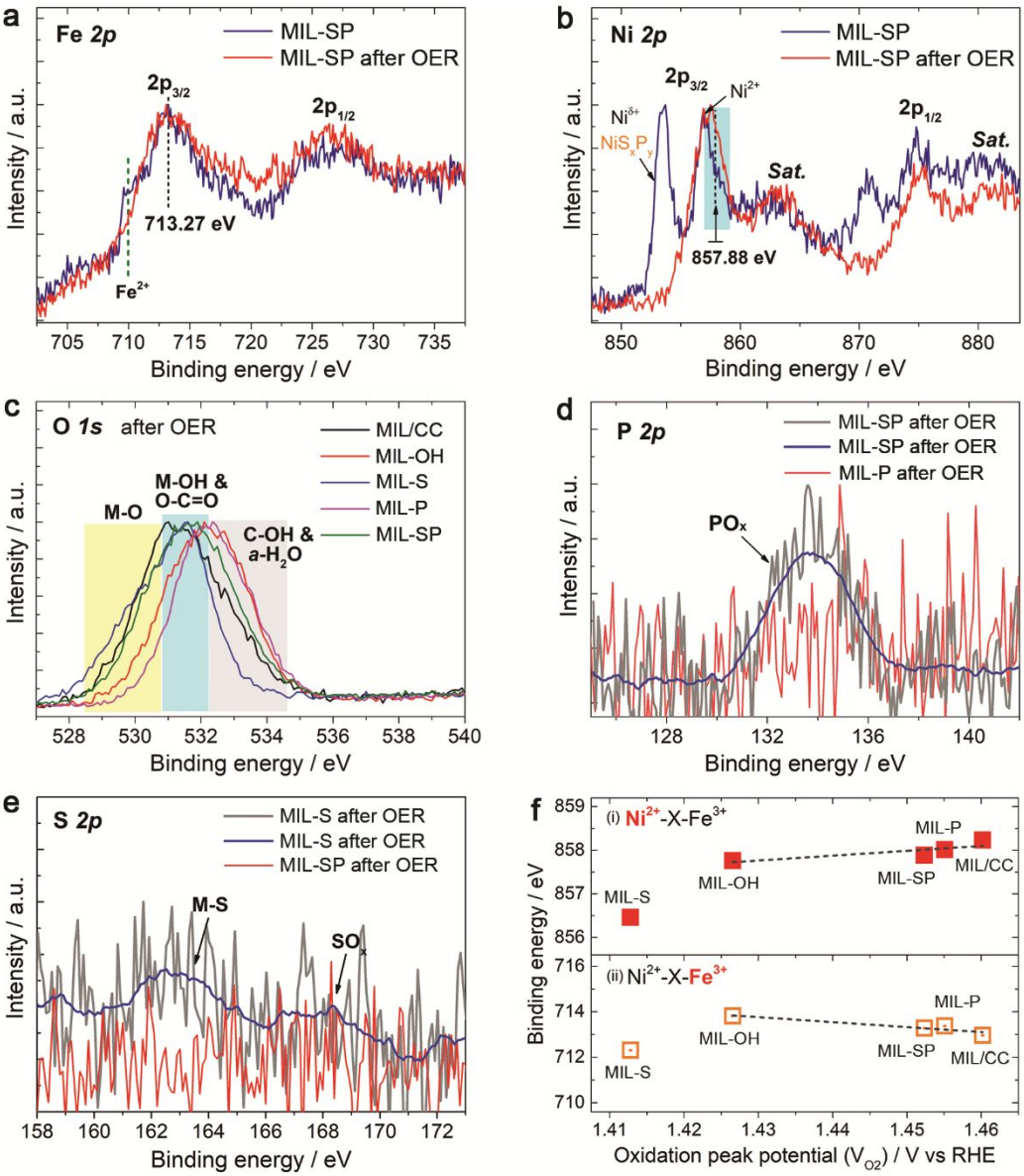

Figure S27. (a, b) Comparison of the Fe 2p and Ni 2p XPS core level spectra of MIL-SP before and after OER tests. (c) O 1s XPS core level spectra of the as-prepared samples after OER. (d) P 2p XPS core level spectra of MIL-P and MIL-SP after OER. (e) S 2p XPS core level spectra of MIL-S and MIL-SP after OER. (f) The relationships between the binding energy (BE) of Ni^{2+}/Fe^{3+} component peaks in Ni^{2+}-X-Fe^{3+} phase after OER tests (X = O, S, P, BDC) and the oxidation peak potentials (V_{O2}) of Ni^{2+}/Ni^{3+} in **Figure S17**. The OER tests here refer to the Chronopotentiometry measurements in **Figure S22**.

For MIL-SP, similarly, it could be found that the reductive Fe^{2+} component (Fe $2p_{3/2}$ spectra, **Figure S27a**) and $Ni^{\delta+}$ (NiS_xP_y)

component (Ni $2p_{3/2}$ spectra, **Figure S27b**) were heavily oxidized after OER tests. However, the main peak position of Fe $2p_{3/2}$ spectra, related to the Fe^{3+} component, is kept at ~713.27 eV before and after OER tests. Besides, the change of Ni^{2+} component peak in Ni $2p_{3/2}$ spectra is also attributed to the increasing content of Ni^{2+}-X-Fe^{3+} phase (at 857.88 eV, light blue area), as discussed in **Figure S25**. Thus, the electronic structures of Fe^{3+} and Ni^{2+} sites in the active Ni^{2+}-X-Fe^{3+} phase of MIL-SP are nearly not changed after OER tests.

In **Figure S27c**, the O 1s spectra reveals the formation of metal oxide and metal hydroxide phases on the surface of the samples after OER tests. Comparatively, the P ligands on the surface of MIL-P and MIL-SP were heavily oxidized and released into electrolyte; the same conditions also occurred on the S ligands of MIL-S and MIL-SP. Nevertheless, for the samples after OER test, the BE of Fe^{3+} and Ni^{2+} sites in the active Ni^{2+}-X-Fe^{3+} phase (except for MIL-S) still exhibits an inverse change tendency with the increasing oxidation peak potential (V_{O2}) of Ni^{2+}/Ni^{3+} (**Figure S27f**), which is almost the same as the conditions before OER tests (**Figure S19** and **Figure S20**). In this case, we suppose that after OER tests, few ligands left on the surface of the samples (*e.g.,* S ligands on MIL-S and P ligands on MIL-SP) or the ligands below the surface layer of the samples could still contribute to tuning the electronic structure of surface Ni/Fe sites in the samples.

To gain insights into the element chemical states below the surface layer of the samples (MIL-S, MIL-P, and MIL-SP) before and after OER tests, depth profiling XPS measurements were further performed via Ar^+ etching (**Figure S28** and **Figure S29**).

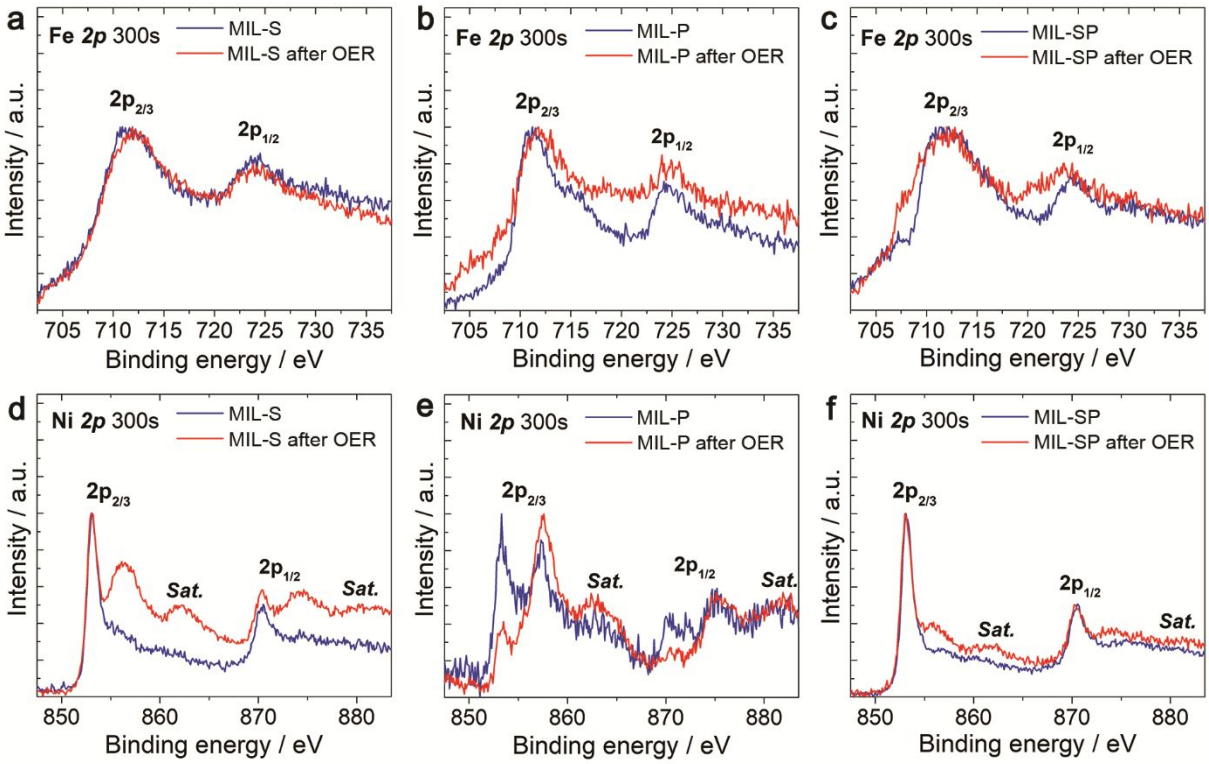

Figure S28. Comparison of the Fe*2p* (a-c) and Ni*2p* (d-f) XPS core level spectra of MIL-S, MIL-P and MIL-SP before (blue line) and after (red line) OER tests, which were recorded after a 5min (300 seconds) Ar^+ etching process.

Obviously, after Ar^+ etching (**Figure S28**), the amounts of reductive Fe^{2+} and $Ni^{\delta+}$ components in the samples are remarkably higher than those on their surface layers (**Figure S25-S27**), no matter before or after OER tests. For the three samples, the Fe *2p* and Ni *2p* XPS spectra recorded after Ar^+ etching is basically retained in the same BE area after OER tests, except for

slightly decreased percentages of reductive Fe^{2+} and $Ni^{\delta+}$ components. Thus, below the surface layer of the samples, the chemical states of their Fe/Ni sites before and after OER tests is almost the same.

In stark contrast, the XPS signal intensity of S and P ligands below the surface layer of the samples apparently declined after OER tests (**Figure S29d and S29f**), which was accompanying with the increasing content of metal oxide phase in MIL-P and MIL-SP (**Figure S29e**).

Based on the above discussions, we can conclude that the electronic structures of Fe/Ni sites in the samples (MIL-S, MIL-P and MIL-SP) can be indeed kept after OER tests, even if a few easily-oxidized ligands (*e.g.,* S and P) are left in the material matrix.

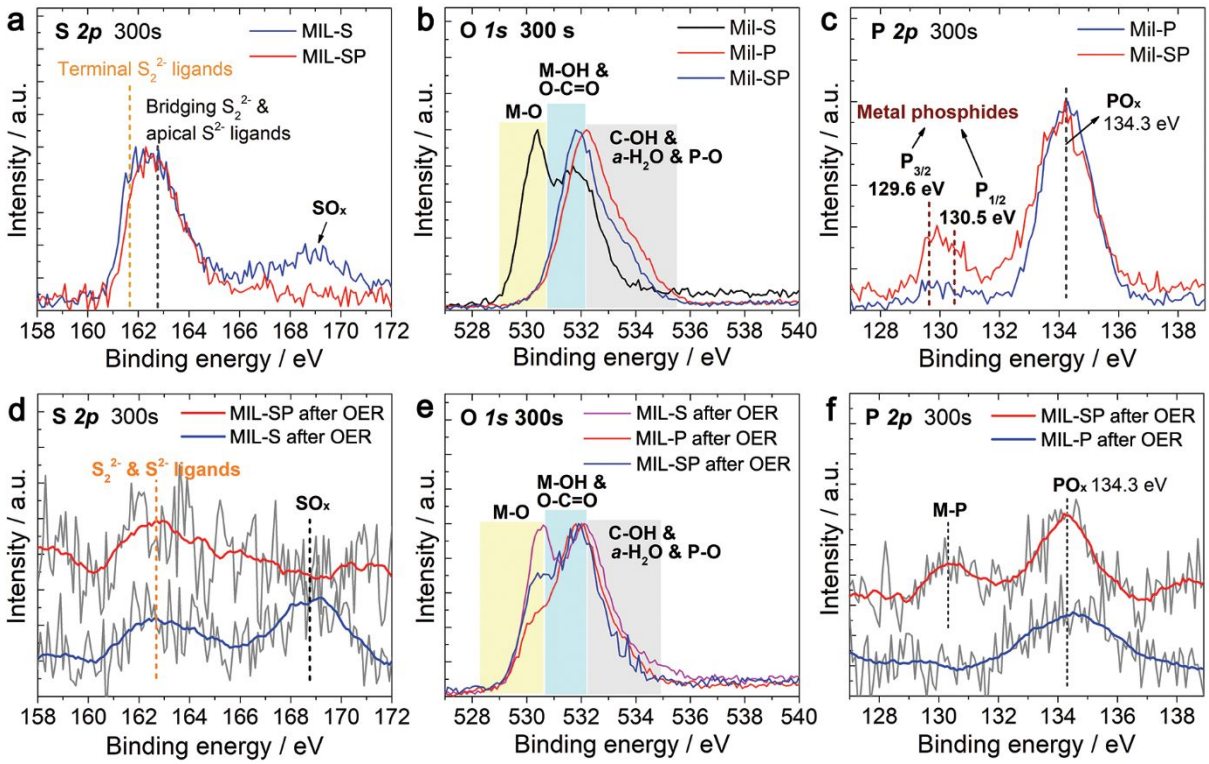

Figure S29. Comparison of the S*2p*, O*1s* and P*2p* XPS core level spectra of MIL-S, MIL-P and MIL-SP before (a-c) and after (d-f) OER tests, which were recorded after a 5min (300 seconds) Ar^{+} etching process.

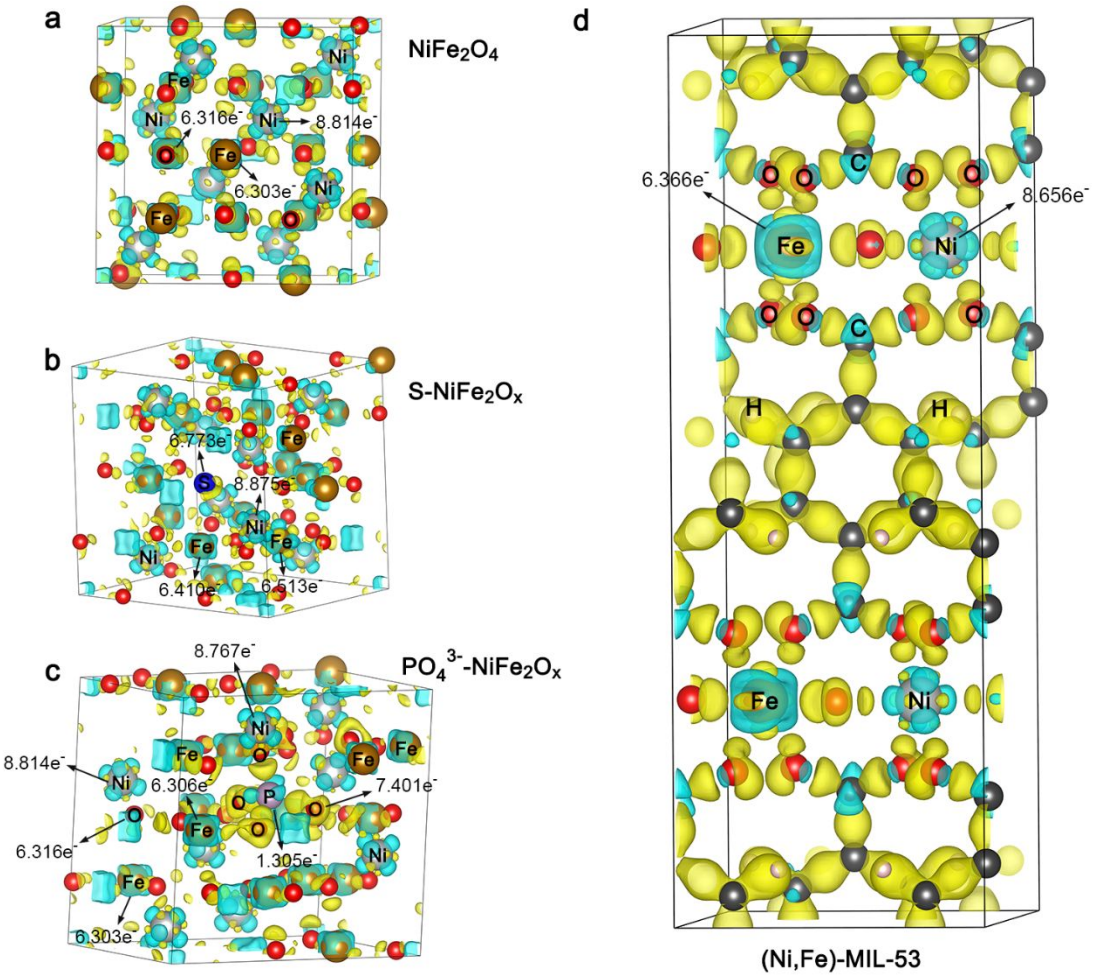

Figure S30. DFT calculations to illustrate charge density distribution and electron transfer from Ni^{2+} to Fe^{3+}. a) Structures and charge distribution of the standard $NiFe_2O_4$ phase, b) and c) structure and charge density distribution of the $NiFe_2O_4$ with one O^{2-} ligand replaced by S^{2-} and PO_4^{3-} ligands, respectively. d) Structure and charge density distribution of (Ni,Fe)-MIL-53. Blue and yellow represent charge depletion and charge accumulation, respectively.

During the OER operation conditions, surface oxidation of the as-prepared catalysts is an unavoidable process, as evidenced by the Raman and XPS analysis (**Figure S5** and **Figure S25-29**). In view of the preferential in-situ formation of active $NiFe_2O_4$ phase on the catalyst surface after catalytic cycling (**Figure S5**), the O^{2-} ligands in $NiFe_2O_4$ were replaced by a series of ligands (S^{2-}, P^{3-}, and PO_4^{3-}) to construct a set of DFT model systems (denoted as S-$NiFe_2O_x$, P-$NiFe_2O_x$, and PO_4^{3-}-$NiFe_2O_x$, respectively, **Figure S30a-c**) for identifying the functions of different ligands. Meanwhile, to elucidate the effects of BDC^{2-} ligands on the electronic structures of Ni^{2+}/Fe^{3+} sites, a (Ni, Fe)-based MIL-53 model was built according to the structural parameters of previously-reported Cr-based MIL-53 MOFs (**Figure S30d**).[38] After introducing S^{2-} and PO_4^{3-} ligands, the system energy of S-$NiFe_2O_x$ (-341.65 eV) and PO_4^{3-}-$NiFe_2O_x$ (-318.36 eV) notably decreased, compared to that of $NiFe_2O_4$ (-178.20 eV), while the introduction of P^{3-} leads to a continuous increase of the system energy (> 0 eV), implying the thermodynamical instability of P-$NiFe_2$Ox. This result suggests that anionic ligand residues (*e.g.,* S^{2-} and PO_4^{3-}) are energetically-preferred in the in-situ forming $NiFe_2O_4$ phase after OER, while the P^{3-} tends to be oxidized upon OER, in good agreement with the XPS results (**Figure S25-29**).

Table S1. Comparison of OER performance (1M KOH) of MIL/CC and MIL-53 derived materials.

Samples	Redox center potential / V_{RHE}	20 mA/cm² @ η [mV]	50 mA/cm² @ η [mV]	100 mA/cm² @ η [mV]	Tafel slope [mV/dec.]
MIL/CC	1.41266	250	274	296	62
MIL-OH	1.37559	245	267	287	54
MIL-S	1.37694	240	259	273	46
MIL-P	1.40414	233	251	264	42
MIL-SP	1.40099	215	242	253	37

Table S2. ICP data of carbon cloth (CC), MIL-53 powder, MIL/CC, and MIL/CC-derived catalysts, and the calculated turnover frequency (TOF) values of the catalysts at overpotential (η) of 270 mV.

Samples	Fe	Ni	Ni/Fe atomic ratio	*J* [mA cm^{-2}] @ η = 270 mV	TOF[a] (Ni) [s^{-1}]	TOF[b] (Ni+Fe) [s^{-1}]
MIL-53 powder	1.969 μmol/mg	2.279 μmol/mg	1.157	--------	--------	--------
MIL/CC	4.011 μmol/cm²	5.651 μmol/cm²	1.409	42.568	0.0195	0.0114
MIL-OH	4.187 μmol/cm²	5.407 μmol/cm²	1.291	58.512	0.0280	0.0158
MIL-S	4.112 μmol/cm²	5.402 μmol/cm²	1.314	83.525	0.0401	0.0227
MIL-P	4.063 μmol/cm²	5.351 μmol/cm²	1.317	133.507	0.0646	0.0367
MIL-SP	4.128 μmol/cm²	5.540 μmol/cm²	1.342	339.077	0.159	**0.0909**
Carbon cloth (CC)	0.007 μmol/cm²	< 0.000	---------	----------	---------	---------

[a] TOF was calculated based on the Ni content; **[b]** TOF was calculated based on the total amount of Fe and Ni atoms.

The turnover frequency (TOF) value was calculated by the following equation: TOF = $10^3 * J/(4F \cdot N)$, where *J* is the current density (mA/cm²) at η = 270 mV, the number 4 means a four-electron OER, F is the Faraday's constant (96485.3329 sA/mol), and N (μmol/cm²) represents the density of metal sites per electrode area, which is determined by the ICP measurements.

The Ni/Fe atomic ratio in MIL/CC (1.409) is a litter higher than that in MIL-53 powders (1.157), which should be ascribed to the Ni-based binders formed in MIL/CC during the EPD process. The Ni atoms from Ni-based binders make up about 17.8% of the total Ni atoms in MIL/CC. Comparatively, the MIL/CC-derived catalysts (MIL-OH, MIL-S, MIL-P, and MIL-SP) exhibit a very close content of Fe and Ni atoms to MIL/CC. This result suggests that most of the metal atoms will be kept after

the EC-MOF and low temperature phosphorization process.

Remarkably, the Ni/Fe atomic ratio (~1.3-1.4) measured by ICP is lower than that measured by EDX (~2.0-2.2), which may be due to the following two reasons: 1) there are more Ni-based binders formed on the surface layer of MIL/CC after the 12 EPD steps (seeing the experimental part and **Figure S2**), because the concentration of MIL-53 powder decreased after each EPD step; 2) the concentration of Ni atoms on the surface of the MIL-53 nanoparticles is higher than that of Fe atoms, because the Fe atoms are easier to form nucleus with BDC ligands than Ni atoms during the solvothermal synthesis of MIL-53. This Ni/Fe ratio difference between ICP and EDX measurements is also found in previously reported NiFe-based MIL-53.[39]

Table S3. The Ni $2p_{3/2}$ fitted peak positions of the as-prepared samples. The corresponding Ni $2p_{3/2}$ fitting curves are shown in Figure 4c and Figure S19. To achieve an effective comparison between different samples, the full width at half maximum values (FWHM) of the same component peak in different samples is kept the same during the simulation.

Ni $2p_{3/2}$ fitting Binding Energy (BE, eV)

Sample	XPS	$Ni(OH)_2/NiS_x/NiS_xP_y$	**Ni^{2+}**-X-Ni^{2+}	**Ni^{2+}**-X-Fe^{3+}	Ni^{2+} Satellite	$Ni(OH)_2$ Satellite
MIL-53 powder	BE	------	856.78	858.23	863.09	-----
	FWHM	------	2.2	2.61	6.18	-----
MIL/CC	BE	855.42	856.76	858.23	862.76	868.88
	FWHM	2.0	2.2	2.61	5.26	1.62
MIL-OH	BE	------	856.08	857.5	862.63	868.73
	FWHM	------	2.2	2.61	5.61	1.62
MIL-S	BE	853.65	855.8	856.7	861.11	------
	FWHM	1.54	2.22	2.61	5.58	------
MIL-P	BE	------	856.9	858.1	862.22	------
	FWHM	------	1.5	2.61	5.82	------
MIL-SP	BE	853.53	856.8	857.88	861.82	------
	FWHM	1.54	1.5	2.61	5.53	------

Table S4. The Fe $2p_{3/2}$ fitted peak positions of the as-prepared samples. The corresponding Fe $2p_{3/2}$ fitting curves are shown in Figure S20. To achieve an effective comparison between different samples, the full width at half maximum values (FWHM)

of the same component peak in different samples is kept the same during the simulation.

Fe $2p_{3/2}$ fitting Binding Energy (BE, eV)						
Sample	XPS	Fe^{2+}	Fe^{3+}	Fe^{3+}	Fe^{2+} Satellite	Fe^{3+} Satellite
MIL-53 Powder	BE	-----	711.88	714.24	-----	718.17
	FWHM	-----	3.5	3.6	-----	2.6
MIL/CC	BE	-----	711.03	713.32	-----	716.87
	FWHM	-----	3.5	3.6	-----	2.6
MIL-OH	BE	-----	711.67	714.05	-----	718.14
	FWHM	-----	3.5	3.6	-----	2.6
MIL-S	BE	710.4	711.52		714.62	718
	FWHM	1.75	3.6		2.0	2.6
MIL-P	BE	710.18	713.23		715.77	717.88
	FWHM	1.75	3.6		2.0	2.6
MIL-SP	BE	710.16	713.08		715.43	717.64
	FWHM	1.75	3.6		2.0	2.6

Table S5. Comparison of OER performance (1M KOH) of the MIL-SP with recently reported state-of-the-art OER catalysts.

Catalysts	**Substrate**	***j* [*mA/cm²*]@ *η* [*mV*]**	**Tafel slope [*mV/dec.*]**	***Ref.***
MIL-SP	Carbon cloth	20@215 50@242 100@253 300@268 500@276	37	**This work**
Gelled FeCoW	Ni foam	10@191 100@~250	37	**40**
$NiFeO_x$	Carbon paper	10@230 50@260 100@~300	31.5	**41**
FeCoNiP nanoparticles on carbon fibers	Glassy carbon	10@200 50@248 100@270	60-120	**27**
$Ni_{1.5}Fe_{0.5}P/CF$	Carbon paper	10@264 50@~279 100@293	55	**42**
$Ni_{0.9}Fe_{0.1}PS$	Glassy carbon	20@329	69	**23**
Ni-Fe LDH hollow nanoprisms	Ni foam	10@295	59	**43**

Fe/Ni2.4/Co0.4-MIL-53/NF	Ni foam	100@238 500@290	71.3	**39**
Ni-Fe-OH@Ni3S2	Ni foam	10@165 100@300 500@530	93	**44**
FeNiP-NP	Ni foam	10@180 20@250 50@300	76	**24**
$Ni_xFe_{1-x}Se_2$-derived oxides	Ni foam	10@195 100@225	28	**45**
Etched bulk NiFeP	Free standing	10@219 100@~300	31-38	**29**
$(Ni_{0.33}Fe_{0.67})_2P$	Ni foam	50@230	55.9	**46**
Se-(NiCo)S/OH	Ni foam	100@~245	33.9	**47**
Ni-MOF@FeMOF	Glassy carbon	10@265	82	**48**
NiFeCr LDH	Carbon paper	25@225	69	**49**
FeOOH/Co/FeOOH	Ni foam	20@250 100@305	33.8	**50**
NiFe-LDH/$Co_{0.85}Se$/EG	Graphene foil	100@270	57	**51**
NiFeV LDHs	Ni foam	10@192 100@~245	42	**52**
NiFeMo	Ni foam	10@238 50@~249	38	**53**
a-NiFe-OH/NiFeP	Ni foam	10@199 50@~230	39	**54**
$W_{0.5}Co_{0.4}Fe_{0.1}$/NF	Ni foam	66.1@300	32	**55**
M-Ni_2P/Fe_2P-O	Ni foam	20@193 50@251 400@379	43.2	**26**
NiTi-MMO	Glassy carbon	10@320	52	**56**
$NiCo_2(SOH)_x$ Nanoflower	Ni foam	10@290	47	**14**

REFERENCES

(1) Liang, R.; Jing, F.; Shen, L.; Qin, N.; Wu, L. MIL-53(Fe) as a highly efficient bifunctional photocatalyst for the

simultaneous reduction of Cr(VI) and oxidation of dyes. *J. Hazard. Mater.* **2015**, *287*, 364-372.

(2) Scheuing, D. R.; Weers, J. G. A Fourier transform infrared spectroscopic study of dodecyltrimethylammonium chloride/sodium dodecyl sulfate surfactant mixtures. *Langmuir* **1990**, *6*, 665-671.

(3) He, W.; Ifraemov, R.; Raslin, A.; Hod, I. Room-Temperature Electrochemical Conversion of Metal–Organic Frameworks into Porous Amorphous Metal Sulfides with Tailored Composition and Hydrogen Evolution Activity. *Adv. Funct. Mater.* **2018**, *28*, 1707244.

(4) Dutcher, B.; Fan, M.; Leonard, B.; Dyar, M. D.; Tang, J.; Speicher, E. A.; Liu, P.; Zhang, Y. Use of Nanoporous FeOOH as a Catalytic Support for NaHCO3 Decomposition Aimed at Reduction of Energy Requirement of Na_2CO_3/$NaHCO_3$ Based CO2 Separation Technology. *J. Phys. Chem. C* **2011**, *115*, 15532-15544.

(5) Grégoire, B.; Ruby, C.; Carteret, C. Hydrolysis of mixed Ni^{2+}–Fe^{3+} and Mg^{2+}–Fe^{3+} solutions and mechanism of formation of layered double hydroxides. *Dalton Trans.* **2013**, *42*, 15687-15698.

(6) Trześniewski, B. J.; Diaz-Morales, O.; Vermaas, D. A.; Longo, A.; Bras, W.; Koper, M. T. M.; Smith, W. A. In Situ Observation of Active Oxygen Species in Fe-Containing Ni-Based Oxygen Evolution Catalysts: The Effect of pH on Electrochemical Activity. *J. Am. Chem. Soc.* **2015**, *137*, 15112-15121.

(7) Louie, M. W.; Bell, A. T. An Investigation of Thin-Film Ni–Fe Oxide Catalysts for the Electrochemical Evolution of Oxygen. *J. Am. Chem. Soc.* **2013**, *135*, 12329-12337.

(8) Zeng, L.; Zhao, T.; Wei, L. Revealing the Performance Enhancement of Oxygenated Carbonaceous Materials for Vanadium Redox Flow Batteries: Functional Groups or Specific Surface Area? *Adv. Sustainable Syst.* **2018**, *2*, 1700148.

(9) Lazarević, Z. Ž.; Jovalekić, Č.; Rečnik, A.; Ivanovski, V. N.; Milutinović, A.; Romčević, M.; Pavlović, M. B.; Cekić, B.; Romčević, N. Ž. Preparation and characterization of spinel nickel ferrite obtained by the soft mechanochemically assisted synthesis. *Mater. Res. Bull.* **2013**, *48*, 404-415.

(10) Lazarević, Z. Ž.; Jovalekić, Č.; Sekulić, D. L.; Milutinović, A.; Baloš, S.; Slankamenac, M.; Romčević, N. Ž. Structural, electrical and dielectric properties of spinel nickel ferrite prepared by soft mechanochemical synthesis. *Mater. Res. Bull.* **2013**, *48*, 4368-4378.

(11) Landon, J.; Demeter, E.; İnoğlu, N.; Keturakis, C.; Wachs, I. E.; Vasić, R.; Frenkel, A. I.; Kitchin, J. R. Spectroscopic Characterization of Mixed Fe–Ni Oxide Electrocatalysts for the Oxygen Evolution Reaction in Alkaline Electrolytes. *ACS Catal.* **2012**, *2*, 1793-1801.

(12) Wei, C.; Feng, Z.; Scherer, G. G.; Barber, J.; Shao-Horn, Y.; Xu, Z. J. Cations in Octahedral Sites: A Descriptor for Oxygen Electrocatalysis on Transition-Metal Spinels. *Adv. Mater.* **2017**, *29*, 1606800.

(13) Cai, P. W.; Huang, J. H.; Chen, J. X.; Wen, Z. H. Oxygen-Containing Amorphous Cobalt Sulfide Porous Nanocubes as High-Activity Electrocatalysts for the Oxygen Evolution Reaction in an Alkaline/Neutral Medium. *Angew. Chem. Int. Ed.* **2017**, *56*, 4858-4861.

(14) Peng, L.; Wang, J.; Nie, Y.; Xiong, K.; Wang, Y.; Zhang, L.; Chen, K.; Ding, W.; Li, L.; Wei, Z. Dual-Ligand Synergistic Modulation: A Satisfactory Strategy for Simultaneously Improving the Activity and Stability of Oxygen Evolution Electrocatalysts. *ACS Catal.* **2017**, *7*, 8184-8191.

(15) Obata, K.; Takanabe, K. A Permselective CeOx Coating To Improve the Stability of Oxygen Evolution Electrocatalysts. *Angew. Chem. Int. Ed.* **2018**, *57*, 1616-1620.

(16) Biesinger, M. C.; Payne, B. P.; Lau, L. W. M.; Gerson, A.; Smart, R. S. C. X-ray photoelectron spectroscopic chemical state quantification of mixed nickel metal, oxide and hydroxide systems. *Surf. Interface Anal.* **2009**, *41*, 324-332.

(17) McIntyre, N. S.; Cook, M. G. X-ray photoelectron studies on some oxides and hydroxides of cobalt, nickel, and copper. *Anal. Chem.* **1975**, *47*, 2208-2213.

(18) Liang, X.; Zheng, B.; Chen, L.; Zhang, J.; Zhuang, Z.; Chen, B. MOF-Derived Formation of Ni2P–CoP Bimetallic

Phosphides with Strong Interfacial Effect toward Electrocatalytic Water Splitting. *ACS Appl. Mater. Inter.* **2017**, *9*, 23222-23229.

(19) Zhang, W.; Qi, J.; Liu, K.; Cao, R. A Nickel-Based Integrated Electrode from an Autologous Growth Strategy for Highly Efficient Water Oxidation. *Adv. Energy Mater.* **2016**, *6*, 1502489.

(20) Dong, C.; Kou, T.; Gao, H.; Peng, Z.; Zhang, Z. Eutectic-Derived Mesoporous Ni-Fe-O Nanowire Network Catalyzing Oxygen Evolution and Overall Water Splitting. *Adv. Energy Mater.* **2018**, *8*, 1701347.

(21) Zhang, W.; Wu, Y. Z.; Qi, J.; Chen, M. X.; Cao, R. A Thin NiFe Hydroxide Film Formed by Stepwise Electrodeposition Strategy with Significantly Improved Catalytic Water Oxidation Efficiency. *Adv. Energy Mater.* **2017**, *7*, 1602547.

(22) Chen, J. S.; Ren, J.; Shalom, M.; Fellinger, T.; Antonietti, M. Stainless Steel Mesh-Supported NiS Nanosheet Array as Highly Efficient Catalyst for Oxygen Evolution Reaction. *ACS Appl. Mater. Inter.* **2016**, *8*, 5509-5516.

(23) Song, B.; Li, K.; Yin, Y.; Wu, T.; Dang, L.; Cabán-Acevedo, M.; Han, J.; Gao, T.; Wang, X.; Zhang, Z.; Schmidt, J. R.; Xu, P.; Jin, S. Tuning Mixed Nickel Iron Phosphosulfide Nanosheet Electrocatalysts for Enhanced Hydrogen and Oxygen Evolution. *ACS Catal.* **2017**, *7*, 8549-8557.

(24) Qian, M.; Cui, S.; Jiang, D.; Zhang, L.; Du, P. Highly Efficient and Stable Water-Oxidation Electrocatalysis with a Very Low Overpotential using FeNiP Substitutional-Solid-Solution Nanoplate Arrays. *Adv. Mater.* **2017**, *29*, 1704075.

(25) Liu, K.; Wang, F.; He, P.; Shifa, T. A.; Wang, Z.; Cheng, Z.; Zhan, X.; He, J. The Role of Active Oxide Species for Electrochemical Water Oxidation on the Surface of 3d-Metal Phosphides. *Adv. Energy Mater.* **2018**, *8*, 1703290.

(26) Liu, P. F.; Li, X.; Yang, S.; Zu, M. Y.; Liu, P.; Zhang, B.; Zheng, L. R.; Zhao, H.; Yang, H. G. Ni2P(O)/Fe2P(O) Interface Can Boost Oxygen Evolution Electrocatalysis. *ACS Energy Lett.* **2017**, *2*, 2257-2263.

(27) Xu, J.; Li, J.; Xiong, D.; Zhang, B.; Liu, Y.; Wu, K.-H.; Amorim, I.; Li, W.; Liu, L. Trends in activity for the oxygen evolution reaction on transition metal (M = Fe, Co, Ni) phosphide pre-catalysts. *Chem. Sci.* **2018**, *9*, 3470-3476.

(28) Ni, B.; He, T.; Wang, J.-o.; Zhang, S.; Ouyang, C.; Long, Y.; Zhuang, J.; Wang, X. The formation of (NiFe)S2 pyrite mesocrystals as efficient pre-catalysts for water oxidation. *Chem. Sci.* **2018**, *9*, 2762-2767.

(29) Hu, F.; Zhu, S. L.; Chen, S. M.; Li, Y.; Ma, L.; Wu, T. P.; Zhang, Y.; Wang, C. M.; Liu, C. C.; Yang, X. J.; Song, L.; Yang, X. W.; Xiong, Y. J. Amorphous Metallic NiFeP: A Conductive Bulk Material Achieving High Activity for Oxygen Evolution Reaction in Both Alkaline and Acidic Media. *Adv. Mater.* **2017**, *29*, 1606570.

(30) Zhuang, L.; Ge, L.; Yang, Y.; Li, M.; Jia, Y.; Yao, X.; Zhu, Z. Ultrathin Iron-Cobalt Oxide Nanosheets with Abundant Oxygen Vacancies for the Oxygen Evolution Reaction. *Adv. Mater.* **2017**, *29*, 1606793.

(31) Görlin, M.; Chernev, P.; Ferreira de Araújo, J.; Reier, T.; Dresp, S.; Paul, B.; Krähnert, R.; Dau, H.; Strasser, P. Oxygen Evolution Reaction Dynamics, Faradaic Charge Efficiency, and the Active Metal Redox States of Ni–Fe Oxide Water Splitting Electrocatalysts. *J. Am. Chem. Soc.* **2016**, *138*, 5603-5614.

(32) Friebel, D.; Louie, M. W.; Bajdich, M.; Sanwald, K. E.; Cai, Y.; Wise, A. M.; Cheng, M.-J.; Sokaras, D.; Weng, T.-C.; Alonso-Mori, R.; Davis, R. C.; Bargar, J. R.; Nørskov, J. K.; Nilsson, A.; Bell, A. T. Identification of Highly Active Fe Sites in (Ni,Fe)OOH for Electrocatalytic Water Splitting. *J. Am. Chem. Soc.* **2015**, *137*, 1305-1313.

(33) Chen, J. Y. C.; Dang, L.; Liang, H.; Bi, W.; Gerken, J. B.; Jin, S.; Alp, E. E.; Stahl, S. S. Operando Analysis of NiFe and Fe Oxyhydroxide Electrocatalysts for Water Oxidation: Detection of Fe^{4+} by Mössbauer Spectroscopy. *J. Am. Chem. Soc.* **2015**, *137*, 15090-15093.

(34) Shin, H.; Xiao, H.; Goddard, W. A. In Silico Discovery of New Dopants for Fe-Doped Ni Oxyhydroxide ($Ni_{1-x}Fe_xOOH$) Catalysts for Oxygen Evolution Reaction. *J. Am. Chem. Soc.* **2018**, *140*, 6745-6748.

(35) Rossmeisl, J.; Qu, Z. W.; Zhu, H.; Kroes, G. J.; Nørskov, J. K. Electrolysis of water on oxide surfaces. *J. Electroanal. Chem.* **2007**, *607*, 83-89.

(36) Man, I. C.; Su, H.-Y.; Calle-Vallejo, F.; Hansen, H. A.; Martínez, J. I.; Inoglu, N. G.; Kitchin, J.; Jaramillo, T. F.; Nørskov, J. K.; Rossmeisl, J. Universality in Oxygen Evolution Electrocatalysis on Oxide Surfaces. *ChemCatChem* **2011**, *3*, 1159-1165.

(37) Klaus, S.; Cai, Y.; Louie, M. W.; Trotochaud, L.; Bell, A. T. Effects of Fe Electrolyte Impurities on Ni(OH)2/NiOOH Structure and Oxygen Evolution Activity. *J. Phys. Chem. C* **2015**, *119*, 7243-7254.

(38) Serre, C.; Millange, F.; Thouvenot, C.; Noguès, M.; Marsolier, G.; Louër, D.; Férey, G. Very Large Breathing Effect in the First Nanoporous Chromium(III)-Based Solids: MIL-53 or CrIII(OH) {O_2C-C_6H_4-CO_2} {HO_2C-C_6H_4-CO_2H}x H_2Oy. *J. Am. Chem. Soc.* **2002**, *124*, 13519-13526.

(39) Li, F.-L.; Shao, Q.; Huang, X.; Lang, J.-P. Nanoscale Trimetallic Metal–Organic Frameworks Enable Efficient Oxygen Evolution Electrocatalysis. *Angew. Chem. Int. Ed.* **2018**, *57*, 1888-1892.

(40) Zhang, B.; Zheng, X.; Voznyy, O.; Comin, R.; Bajdich, M.; García-Melchor, M.; Han, L.; Xu, J.; Liu, M.; Zheng, L.; García de Arquer, F. P.; Dinh, C. T.; Fan, F.; Yuan, M.; Yassitepe, E.; Chen, N.; Regier, T.; Liu, P.; Li, Y.; De Luna, P.; Janmohamed, A.; Xin, H. L.; Yang, H.; Vojvodic, A.; Sargent, E. H. Homogeneously dispersed multimetal oxygen-evolving catalysts. *Science* **2016**, *352*, 333-337.

(41) Wang, H.; Lee, H.-W.; Deng, Y.; Lu, Z.; Hsu, P.-C.; Liu, Y.; Lin, D.; Cui, Y. Bifunctional non-noble metal oxide nanoparticle electrocatalysts through lithium-induced conversion for overall water splitting. *Nat. Commun.* **2015**, *6*, 7261.

(42) Huang, H.; Yu, C.; Zhao, C.; Han, X.; Yang, J.; Liu, Z.; Li, S.; Zhang, M.; Qiu, J. Iron-tuned super nickel phosphide microstructures with high activity for electrochemical overall water splitting. *Nano Energy* **2017**, *34*, 472.

(43) Yu, L.; Yang, J. F.; Guan, B. Y.; Lu, Y.; Lou, X. W. Hierarchical Hollow Nanoprisms Based on Ultrathin Ni-Fe Layered Double Hydroxide Nanosheets with Enhanced Electrocatalytic Activity towards Oxygen Evolution. *Angew. Chem. Int. Ed.* **2018***, 57,* 172.

(44) Zou, X.; Liu, Y. P.; Li, G. D.; Wu, Y. Y.; Liu, D. P.; Li, W.; Li, H. W.; Wang, D. J.; Zhang, Y.; Zou, X. X. Ultrafast Formation of Amorphous Bimetallic Hydroxide Films on 3D Conductive Sulfide Nanoarrays for Large-Current-Density Oxygen Evolution Electrocatalysis. *Adv. Mater.* **2017**, *29*, 1700404.

(45) Xu, X.; Song, F.; Hu, X. A nickel iron diselenide-derived efficient oxygen-evolution catalyst. *Nat. Commun.* **2016**, *7*, 12324.

(46) Li, Y.; Zhang, H.; Jiang, M.; Zhang, Q.; He, P.; Sun, X. 3D Self-Supported Fe-Doped Ni_2P Nanosheet Arrays as Bifunctional Catalysts for Overall Water Splitting. *Adv. Funct. Mater.* **2017**, *27*, 1702513.

(47) Hu, C.; Zhang, L.; Zhao, Z.-J.; Li, A.; Chang, X.; Gong, J. Synergism of Geometric Construction and Electronic Regulation: 3D Se-$(NiCo)S_x/(OH)_x$ Nanosheets for Highly Efficient Overall Water Splitting. *Adv. Mater.* **2018**, *30*, 1705538.

(48) Rui, K.; Zhao, G.; Chen, Y.; Lin, Y.; Zhou, Q.; Chen, J.; Zhu, J.; Sun, W.; Huang, W.; Dou, S. X. Hybrid 2D Dual-Metal-Organic Frameworks for Enhanced Water Oxidation Catalysis. *Adv. Funct. Mater.* **2018**, *28*, 1801554.

(49) Yang, Y.; Dang, L.; Shearer, M. J.; Sheng, H.; Li, W.; Chen, J.; Xiao, P.; Zhang, Y.; Hamers, R. J.; Jin, S. Highly Active Trimetallic NiFeCr Layered Double Hydroxide Electrocatalysts for Oxygen Evolution Reaction. *Adv. Energy Mater.* **2018**, *8*, 1703189.

(50) Feng, J.-X.; Xu, H.; Dong, Y.-T.; Ye, S.-H.; Tong, Y.-X.; Li, G.-R. FeOOH/Co/FeOOH Hybrid Nanotube Arrays as High-Performance Electrocatalysts for the Oxygen Evolution Reaction. *Angew. chem. Int. Ed.* **2016**, *128*, 3694.

(51) Hou, Y.; Lohe, M. R.; Zhang, J.; Liu, S.; Zhuang, X.; Feng, X. Vertically oriented cobalt selenide/NiFe layered-double-hydroxide nanosheets supported on exfoliated graphene foil: an efficient 3D electrode for overall water splitting. *Energy Environ. Sci.* **2016**, *9*, 478.

(52) Li, P.; Duan, X.; Kuang, Y.; Li, Y.; Zhang, G.; Liu, W.; Sun, X. Tuning Electronic Structure of NiFe Layered Double Hydroxides with Vanadium Doping toward High Efficient Electrocatalytic Water Oxidation. *Adv. Energy Mater.* **2018**,

8, 1703341.

(53) Qin, F.; Zhao, Z.; Alam, M. K.; Ni, Y.; Robles-Hernandez, F.; Yu, L.; Chen, S.; Ren, Z.; Wang, Z.; Bao, J. Trimetallic NiFeMo for Overall Electrochemical Water Splitting with a Low Cell Voltage. *ACS Energy Lett.* **2018**, *3*, 546-554.

(54) Liang, H.; Gandi, A. N.; Xia, C.; Hedhili, M. N.; Anjum, D. H.; Schwingenschlögl, U.; Alshareef, H. N. Amorphous NiFe-OH/NiFeP Electrocatalyst Fabricated at Low Temperature for Water Oxidation Applications. *ACS Energy Lett.* **2017**, *2*, 1035.

(55) Pi, Y.; Shao, Q.; Wang, P.; Lv, F.; Guo, S.; Guo, J.; Huang, X. Trimetallic Oxyhydroxide Coralloids for Efficient Oxygen Evolution Electrocatalysis. *Angew. Chem. Int. Ed.* **2017**, *56*, 4502.

(56) Zhao, Y.; Jia, X.; Chen, G.; Shang, L.; Waterhouse, G. I. N.; Wu, L.-Z.; Tung, C.-H.; O'Hare, D.; Zhang, T. Ultrafine NiO Nanosheets Stabilized by TiO2 from Monolayer NiTi-LDH Precursors: An Active Water Oxidation Electrocatalyst. *J. Am. Chem. Soc.* **2016**, *138*, 6517.